Latent Space-Driven Quantification of Biofilm Formation using Time Resolved Droplet Microfluidics

Daniela Pérez Guerrero, Jesús Manuel Antúnez Domínguez, Aurélie Vigne, Daniel Midtvedt, Wylie Ahmed, Lisa D. Muiznieks, Giovanni Volpe, Caroline Beck Adiels

Microchemical Journal 225 (2026) 117685

Contents lists available at ScienceDirect

Microchemical Journal

journal homepage: www.elsevier.com/locate/microc

Latent space-driven quantification of biofilm formation using time-resolved droplet microfluidics

Daniela Pérez Guerrero [a,1], Jesús Manuel Antúnez Domínguez [a,b,1], Aurélie Vigne [b], Daniel Midtvedt [a], Wylie W. Ahmed [c,d,e], Lisa D. Muiznieks [b], Giovanni Volpe [a,f], Caroline Beck Adiels [a,*]

[a] University of Gothenburg, Physics Department, Origovägen 6 B, Gothenburg, 412 58, Sweden
[b] Microfluidics Innovation Center, 172 Rue de Charonne, Paris, 75011, France
[c] Université de Toulouse, CNRS, Laboratoire de Physique Théorique, 118 Rte de Narbonne, Toulouse, 31062, France
[d] Université de Toulouse, CNRS, Centre de Biologie Intégrative, 118 Rte de Narbonne, Toulouse, 31062, France
[e] Department of Physics, California State University Fullerton, 800 N. State College Blvd, 92831, CA, USA
[f] Science for Life Laboratory, Physics Department, University of Gothenburg, Gothenburg, Sweden

ARTICLE INFO

MSC:
0000
1111

Keywords:
Biofilm formation
Unsupervised segmentation
Droplet microfluidics
Microscopy
Variational autoencoder
High-throughput screening

ABSTRACT

Bacterial biofilms play crucial roles across diverse contexts, from public health risks to beneficial applications in bioremediation, biodegradation, and wastewater treatment. However, tools that enable high-resolution, dynamic analysis of their responses to environmental cues and collective cellular behaviors remain limited. Here, we present a droplet-based microfluidic platform that combines continuous in situ microscopy with subsequent unsupervised deep learning for quantitative analysis of biofilm development. In our setup, *Bacillus subtilis* cells are encapsulated in monodisperse aqueous microdroplets containing Lysogeny Broth, suspended in an oil phase and immobilized within microfabricated traps, providing continuous optical access throughout biofilm formation at the water–oil interface. The platform supports both fluorescence and bright-field imaging, enabling high-throughput, time-resolved monitoring of thousands of droplets under controlled conditions. To extract quantitative information from these large datasets, we developed an automated analysis pipeline based on a Variational Autoencoder (VAE) trained directly on microscopy images from our experiments. This unsupervised model enables segmentation and latent-space representation of bacterial structures without manual annotation or synthetic training data. Post-segmentation size thresholding enables classification of bacterial aggregates and larger biofilm-like clusters, including quantification of biofilm porosity, thereby supporting detailed morphological and temporal analyses across droplets and conditions. By integrating droplet microfluidics with unsupervised deep learning, our platform provides a scalable, robust, and rapid approach for high-throughput quantitative studies of biofilm behavior. It resolves complex structural biofilm patterns, bypasses the need for manual annotation, and opens new opportunities to probe environmental determinants of biofilm formation. Departing from earlier methods, our framework fuses biological training data with unsupervised models to quantify microbial community dynamics across scales, offering a generalizable platform for future high-resolution microbiology.

1. Introduction

Bacteria, despite their small size, are highly adaptable organisms that rely on complex collective behaviors to withstand hostile environmental conditions [1]. These behaviors emerge from their capacity to move through their surroundings [2,3] and communicate via quorum sensing [4], enabling association and synchronization. Biofilm formation is one of the most prominent examples of such collective behavior. In this state, cells embed themselves in an extracellular matrix (ECM) that anchors them to the interface between two media [5]. The biofilm structure promotes close cell-to-cell interactions and task differentiation, such as the emergence of motile scouts or recalcitrant cells like endospores [6].

* Corresponding author.
E-mail address: caroline.adiels@physics.gu.se (C. B. Adiels).
[1] These authors contributed equally to this work.

https://doi.org/10.1016/j.microc.2026.117685
Received 3 December 2025; Received in revised form 2 March 2026; Accepted 11 March 2026
Available online 6 April 2026

This organization enhances bacterial resistance to environmental stressors, including predation [7], desiccation [8], and antibiotics [9]. In the case of antibiotics, biofilms contribute to resistance by facilitating genetic exchange and promoting collective tolerance [10,11]. While they present challenges in healthcare (e.g., persistent infections and sterilization difficulties [12]), biofilms also have beneficial applications in bioremediation and biotechnology [13] due to their unique metabolic capabilities.

Most experimental biofilm studies rely on bulk culture systems such as agar and well plates, or on substrate-based systems analyzed *ex situ*, including the Modified Robbins Device [14] and the drip-flow biofilm reactor [15]. However, these methods disrupt the native environment and prevent real-time observation [16]. In contrast, microfluidics offers an alternative platform for microbiological studies [17], enabling *in situ* visualization through transparent microfluidic chips.

Over the past decade, microfluidic technology has transformed biomedical and clinical applications through precise microscale fluid control, reduced sample requirements, rapid analysis, and enhanced sensitivity. Recent reviews highlight its expanding role in diagnostics, monitoring, and treatment, underscoring its broad impact across healthcare disciplines [18,19].

When designed with two immiscible liquid phases, microfluidic systems can produce droplets—discrete, compartmentalized environments that mimic isolated microhabitats. Each droplet functions as an individual experimental unit within an emulsion-like suspension, allowing for parallelization and high-throughput data generation [20,21].

Droplet microfluidics in particular has emerged as a powerful technology for high-throughput single-cell analysis, enabling the encapsulation of individual cells within nanoliter- to picoliter-scale reactors that support detailed phenotypic and genomic investigation [22]. These droplet-based platforms allow controlled single-cell screening, studies of intercellular interactions, and scalable biological assays, while also raising practical considerations regarding throughput, system integration, and standardization [22]. They have also been applied to investigate microbial behavior, including that of *B. subtilis*, in well-defined droplet microenvironments. For example, Chang et al. [23] introduced monodisperse emulsion drops as 3D microenvironments for *B. subtilis* growth and visualized structural differentiation within each drop. More recently, Tang et al. [24] used droplet microfluidics and confocal imaging to track *B. subtilis* clustering and motility near the droplet interface, finding that cells preferentially localize at droplet surfaces. In parallel, droplet-based systems have also been employed to study microbial community dynamics, single-cell physiology, and high-throughput culture assays [20,21,23], establishing droplets as powerful platforms for probing bacterial physiology in controlled microhabitats. The integration of artificial intelligence (AI) with droplet microfluidics further expands the analytical capabilities of these systems. Recent advances demonstrate how AI-driven approaches can optimize droplet generation, material synthesis, and biological analysis, enabling intelligent system control and high-dimensional data interpretation [25,26]. High-throughput microfluidic platforms increasingly rely on machine learning to process multimodal datasets — including images, videos, and electrical signals — thus accelerating biomedical detection, drug screening, and automated system design [27].

Despite the growing adoption of droplet-based systems, quantitative image analysis of bacterial structures remains a major challenge. Most existing segmentation workflows rely on supervised deep-learning models such as U-Nets [28–30] or convolutional neural networks (CNNs) [31], which require extensive pixel-level annotations and perform best under well-controlled imaging conditions. For example, recent studies applying U-Net or DeepLabv3+ architectures to bright-field or SEM datasets have reported moderate to strong segmentation performance [29,30,32], while frameworks such as MiSiC [28] have focused primarily on qualitative evaluation for phase-contrast and fluorescence images. In volumetric contexts, approaches such as BCM3D and its subsequent semi-supervised extension [31,33] have demonstrated the feasibility of segmenting 3D fluorescence biofilms, although these methods still rely on curated annotations or extensive manual parameter tuning.

Beyond supervised segmentation, deep learning has increasingly enabled label-free bio-imaging and automated droplet classification. Light-scattering-based droplet screening platforms now permit label-free single-cell detection within microdroplets by minimizing refractive index mismatch, reducing reliance on fluorescence labeling [34]. Deep neural networks such as ResNet architectures have been successfully applied to classify cell-containing droplets in microscopy images with high accuracy, even in complex functional assays [35]. More broadly, AI-assisted microfluidic bio-imaging integrates advanced imaging sensors with machine learning algorithms for super-resolution, classification, and detection tasks, significantly enhancing high-throughput image analysis [36]. Recent reviews further emphasize the role of deep learning in label-free image processing, cell state classification, regression analysis, and generative modeling to improve reproducibility and scalability in single-cell studies [37].

While supervised and semi-supervised pipelines have substantially advanced bacterial image analysis, their reliance on annotated training data or manual tuning limits scalability and reproducibility—particularly for high-throughput droplet assays where hundreds to thousands of images must be processed. Unsupervised deep-learning models offer a compelling alternative by learning intrinsic structural features directly from experimental data, reducing the need for annotated datasets and enabling more consistent segmentation across diverse imaging conditions.

To bridge this methodological gap between high-throughput droplet imaging and scalable, annotation-free analysis, we developed a workflow that combines droplet-based microfluidics with unsupervised deep learning. In this framework, biofilm-forming bacteria are inoculated in the aqueous phase of microfluidic droplets, enabling high-throughput imaging of self-contained microenvironments. Each droplet acts as a miniature culture from which we collect detailed microscopy data from hundreds of droplets. To efficiently process and analyze the resulting large and complex image dataset, we employ Variational Autoencoders (VAEs) [38,39], which learn to represent intricate image structures in an unsupervised manner without requiring annotated datasets.

In our implementation, the VAE is trained directly on microscopy images from the droplet experiments, enabling it to learn structural features inherent to the biological system without reliance on manual annotations or synthetic data.

The VAE architecture comprises an encoder that compresses image crops into a low-dimensional latent space and a decoder that reconstructs them. In this work, we bypass the decoder and operate directly in the latent space, where spatial and structural features are encoded, enabling automated segmentation and quantitative feature extraction without the need for image reconstruction. This strategy provides an efficient and scalable approach for analyzing high-throughput datasets.

In this work, we demonstrate the platform with fluorescence and bright-field microscopy, maintaining temporal synchronization with droplet generation. The VAE efficiently processes the resulting large-scale time-lapse datasets, allowing automated segmentation and quantitative analysis of bacterial structural organization. A subsequent size-based thresholding step further enables quantification of smaller bacterial aggregates, larger biofilm-like clusters, and the porosity of biofilm structures.

Finally, the microfluidic system enables controlled variation of environmental parameters, such as nutrient availability and chemical treatments, that shape bacterial community development. Combined with optical time-lapse microscopy and unsupervised deep learning–based image analysis, this integrated platform provides a robust and scalable framework for high-throughput, quantitative investigation of bacterial community behavior under defined microenvironmental conditions.

2. Materials and methods

2.1. Bacterial strain

The genetically modified fluorescent strain *Bacillus subtilis* MTC871 (modifications stated in SI, Appendix A) was used as the model organism. This strain exhibits red fluorescence when motile, blue fluorescence in the matrix-forming state, and green fluorescence when forming endospores. The strain was grown in Lysogeny Broth Lennox medium (Sigma-Aldrich, Germany) at the optimal growth temperature [40], 37°C, until the OD_{600} reading of the culture was stable (OD_{600} = 1.0). To assess the reproducibility and repeatability of the experiments, the growth curve of *Bacillus subtilis* and the relation between the OD of a sample and bacterial concentration were established using the spread plate technique (see SI Appendix A, Fig. A.1 and Fig. A.2.) Bacillus subtilis (in a concentration of OD_{600} = 0.06) were inoculated in Falcon reservoirs filled with Lysogeny Broth (LB) medium. One reservoir was kept sterile as a negative control to generate empty droplets. Reagents were added to assess their impact on biofilm formation. The effects of Penicillin/Streptomycin (Pen/Strep, 5000 units of penicillin and 5 mg streptomycin per 1 mL, Sigma-Aldrich, Germany) at concentrations ranging from 0 to 4 μL per 1 mL of medium, as well as filter-sterilized glycerol (Dutscher, France) at a fixed concentration of 1% (v/v), were investigated within the droplets.

2.2. Droplet-based microfluidic platform

Each droplet functions as a self-contained microenvironment, making it essential that all components involved — surfactant, oil, aqueous phase, chip substrate, and analysis techniques — are carefully selected and tuned in harmony. In this context, where the species of interest were encapsulated within individual droplets, the biocompatibility of every element becomes crucial. The continuous phase consisted of HFE-7500 perfluorinated oil (Novec7500, 3M) with a 1% (w/w) concentration of Fluorosurf surfactant (Emulseo, France). The negative control, bacterial suspensions, and continuous phase reservoirs were connected to a pressure pump OB1 (Elveflow, France) to accurately control the liquid injection into the chip and coupled with flow sensors, MFS2D (Elveflow, France) for the dispersed phase and MFS3D (Elveflow, France) for the continuous phase. A diagram of the complete setup can be found in SI Appendix B, Fig. B.3. The pressure pump can establish a feedback loop to allow precise control of the liquid flow rate. Teflon tubing with an outer diameter of 1/32″ and inner diameter of 300 μm (Darwin Microfluidics, France) was used to connect all the fluidic parts. To properly control the dispersed phase, 20 cm of 100 μm inner diameter resistance tubing (Elveflow, France) was added to the platform after the flow sensor. A rotary multi-injection valve (MUX distributor from Elveflow, France) was added to allow the permutation of the dispersed solutions (negative control and bacterial suspensions) within the same chip. The sequence of measured solutions was spaced with pure perfluorinated oil included in the multi-injection valve channels to prevent the mixing of consecutive solutions, as shown in SI, Appendix B, Fig. B.3.

2.3. Microfluidic chip

A microfluidic chip (Fluidic 719, Microfluidic Chipshop, Germany) fabricated from the cyclo-olefin copolymer Topas was used for droplet generation. The dispersed and continuous phases were introduced through separate inlets into a flow-focusing geometry with an 82 μm nozzle (SI Appendix B, Fig. B.3). The resulting droplets were directed into a serpentine channel containing microfabricated traps. Before each experiment, the channels were treated with Aquapel [41] and rinsed with the continuous phase to promote dewetting of the dispersed phase and prevent droplet coalescence. Droplet formation was controlled by adjusting the flow rates, with the continuous phase set to 35 μL/min and the dispersed phase to 2 μL/min. This configuration produces highly monodisperse droplets with a diameter of approximately 150 μm (CV = 2%), corresponding to a volume of ~1.7 nL (SI Appendix C, Fig. C.4). Monodispersity served as the primary control parameter to ensure equivalence across droplets.

The droplets were generated from a bacterial suspension with an initial OD_{600} = 0.06, yielding an estimated 14 CFU (Colony Forming Units) per droplet based on the calibration curve, which we take as an approximation of the number of bacteria encapsulated per droplet.

Along the serpentine channel, which has a height of 110 μm, a total of 2261 droplet traps were alternatively positioned on each side. Each trap has a diameter of 173 μm and an additional height of 80 μm. The aqueous phase droplets, less dense than the perfluorinated oil, float in the serpentine channel and become stuck in the traps, preventing their displacement, as illustrated in SI Appendix B, Fig. B.3. Given the size of the droplets, only one droplet can be contained in each trap, and the rest dodge it and continue their trajectory until they reach the next free trap or the chip outlet. However, droplets can be replaced or pushed out from their trap at high flow rates. The dispersed phase flow was stopped once the reagent sequence was finished, while the continuous phase flow continued until all the droplets were trapped. Once the desired number of traps was filled, low-volume displacement plugs (Microfluidic Chipshop, Germany) were used to seal the inlets, preventing evaporation.

2.4. Biofilm observation

The chip architecture provided stationary and stable bacteria-containing droplets, which were monitored over time as shown in Fig. 1A. Intra-droplet pellicle formation was triggered at the oil-liquid interfaces of the droplet surface due to the high oxygen permeability of the oil, (further experimental evidence is provided in SI, Appendix D). This process was monitored using either fluorescence or bright-field time-lapse microscopy, as described below.

2.4.1. Fluorescence microscopy

To evaluate the platform's performance in assessing antibiotic effects on bacterial cultures, fluorescence microscopy time-lapse imaging was performed on 2000 droplets. Two fluorescence channels were used: Texas Red, detecting motile cells expressing the *mKate* fluorophore linked to flagellin production (peak excitation/emission at 572/629 nm), and FITC, detecting endospore formation via the *citrus* fluorophore linked to PsspB protein production (peak excitation/emission at 500/535 nm). The fluorescent reporter for matrix production, based on Cyan Fluorescent Protein (CFP), was not employed in this study due to the photo-toxic effects of its excitation wavelength (approximately 430–435 nm), which can induce cell death or physiological stress [42,43]. This effect is illustrated in the SI Video 1 and 2, showing a droplet before and after irradiation. Accordingly, the CFP reporter was never utilized in our experiments. Moreover, no fluorescent measurements were performed during time-lapse acquisitions to avoid potential loss of viability, stage-dependent effects, or other light-dependent biases [44].

2.4.2. Bright-field microscopy

Two different approaches were used for bright-field microscopy measurements: a low-throughput and a high-throughput setup. The low-throughput time-lapse imaging of a few droplets at short acquisition intervals was used to establish an automated VAE-based image analysis model and reference for biofilm formation dynamics. Images were acquired using an inverted microscope (DMi 6000B; Leica Microsystems, Wetzlar, Germany) equipped with a SOLA III U-nIR LED source (Lumencor, Beaverton, USA) and a Hamamatsu Orca Flash 4 camera (Hamamatsu Photonics, Kista, Stockholm). Six droplets were automatically imaged at 63x magnification every 7 min for 17.5 h.

A total of 676 trapped droplets were manually imaged at defined time intervals to monitor biofilm development using a compound light microscope at 40x magnification (Microscope Axio Vert.A1 TL/RL, Carl Zeiss AG, ZEISS, Germany).

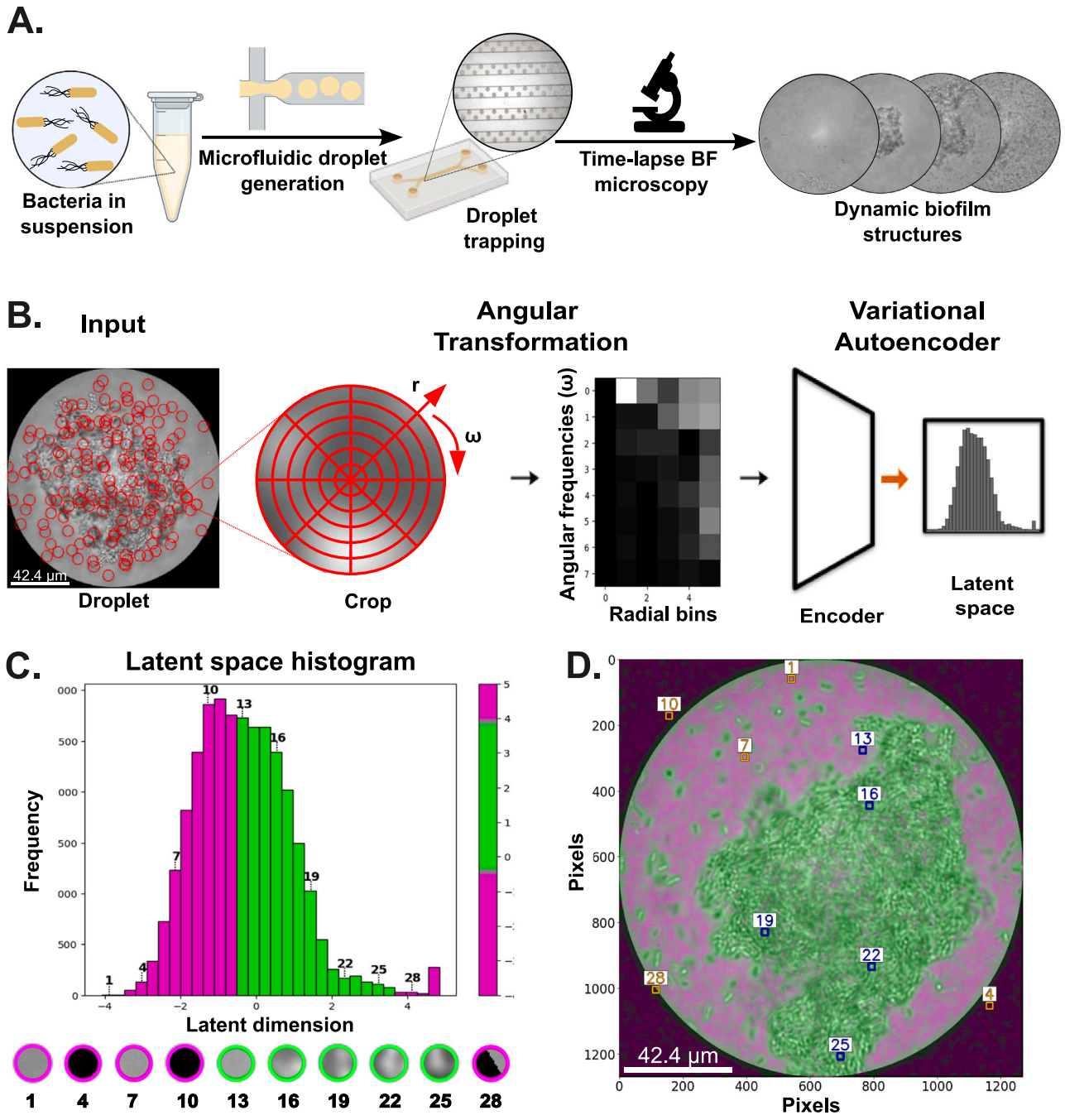

Fig. 1. Droplet analysis pipeline and latent space visualization of biofilm images. A. In the experimental process, a freshly inoculated bacterial suspension produces and stabilizes droplets inside a microfluidic chip. The development and change of biofilm structures were observed *in situ* using bright-field timelapse microscopy. B. The image processing pipeline includes droplet detection, random cropping, and the angular transformation, which prepare the bright-field images for analysis using the Variational Autoencoder. The processed images serve as the input for feature extraction. C. The histogram represents the latent space of the trained VAE. The chosen color code helps distinguish the droplet background from bacterial structures. Representative elements from different bins along the latent space illustrate the progression from an empty crop to the early formation of biofilm and then to more complex structures. D. Visual overlay generated by passing the droplet through the trained VAE using a structured grid. Representative crops from selected histogram bins are overlaid to show their spatial positions within the droplet.

2.5. Image analysis

Fluorescence images were quantified by measuring the emission intensity within each droplet. The mean intensity of each droplet was calculated, and each wavelength channel was normalized to the highest mean value across all batches. The resulting normalized intensities were plotted as a function of antibiotic concentration. The experiment was repeated four times, analyzing more than 500 droplets of each type in total.

Bright-field images were analyzed using an unsupervised learning approach based on a VAE. The latent space representation was used to map structural patterns within the images, enabling detailed characterization of bacterial structures. These images were acquired with the compound light microscope and were resized to a fixed resolution

of 256 × 256 pixels. The droplets were detected as circular features using the Hough Circle Transform, an algorithm for identifying circular shapes and defining the droplet area.

The detected droplets were cropped to a reduced radius of 4/5 of the original to isolate the core region, followed by the application of a Gaussian-blurred mask to create smooth boundaries. The processed images were then converted to grayscale. In contrast, time-lapse bright-field images acquired with the inverted microscope were at their original resolution, focusing solely on detecting circular features using the Hough Circle Transform approach.

The VAE models were trained directly on microscopy images obtained from droplet experiments, without using synthetic data or manual annotations. Two representative grayscale images per setup were selected: one showing a well-structured biofilm and another displaying a dispersed, planktonic population. Because the VAE learns to represent image features without pre-labeled data, the training was fully unsupervised, allowing the model to capture intrinsic structural variation within the biological samples. A separate model was trained for each microscopy setup to account for differences in illumination and imaging conditions.

To enhance spatial diversity and improve pattern recognition, 10,000 random crops with a radius of 12 pixels were extracted from each training image. The crop radius was selected as a compromise between spatial specificity, robustness to label-free bright-field (BF) texture variability, and computational efficiency. Smaller crops increase spatial resolution but are more sensitive to local intensity fluctuations and acquisition artifacts (e.g., illumination non-uniformity and boundary shading), which can increase false positives, whereas larger crops provide more context but may mix biofilm and background and oversmooth thin or faint structures. To relate this choice to the physical scale of bacteria in our images, we estimated single-cell dimensions in pixel units from representative BF frames using Fiji/ImageJ rectangular ROIs ($n = 50$). The measured bounding-box dimensions were Width = 12.55 ± 2.48 px and Height = 12.88 ± 1.86 px (mean ± SD; medians 12 px and 13 px; ranges Width 10–27 px, Height 10–18 px), indicating that a crop radius of 12 px is well matched to the characteristic per-cell texture scale. Because bacteria are rod-shaped, capturing the short-axis (cell width) texture scale is often sufficient for local recognition even if the full cell length extends beyond a single crop; longer structures are represented across neighboring regions through the overlapping sampling used during reconstruction. Having defined the crop radius, the extracted crops were then transformed into a radial coordinate system to achieve rotation-invariant learning, enabling the model to focus on structural rather than orientational features. To further reduce sensitivity to cell orientation, these crops were transformed into a radial coordinate system to achieve rotation-invariant learning, enabling the model to focus on structural rather than orientational features. Specifically, the transformation performed a polar Fourier decomposition, where angular harmonics were analyzed within radial bins. This yields a compact encoding of angular and radial spatial frequencies, from which the VAE learns meaningful, orientation-independent representations. A visual overview of this preprocessing pipeline is shown in Fig. 1B.

The VAE architecture was designed to encode the bright-field image representation into a one-dimensional latent variable. The encoder and decoder each comprised two 1D convolutional blocks with channel widths [32, 64] (no pooling/upsampling), using LeakyReLU activations (negative slope 0.1), Identity normalization, and dropout 0.1 in intermediate blocks. The latent dimension was set to 1, parameterized by fully connected layers producing μ and σ^2 of the approximate posterior, and the decoder used a corresponding fully connected mapping followed by convolutional decoding; the final decoder output employed a Sigmoid activation.

Training the VAE model consists of (i) a reconstruction term computed using Binary Cross Entropy loss (BCELoss, reduction = "sum") and (ii) a Kullback–Leibler divergence regularization term weighted by $\beta = 1.0$. Optimization was performed using Adam with a learning rate of 0.002 for 1000 epochs. The model was implemented in PyTorch/Lightning using the Deeplay framework [45], and training was executed on an MPS-accelerated backend (Apple Metal Performance Shaders). Full implementation details, including the exact fully connected mappings used for μ, σ^2, and decoder preprocessing for the 8×8 input representation, are provided in SI Appendix E. After training, the encoder extracted a single latent variable from each crop, generating compressed representations that captured key image features for downstream analysis. The distribution of these features was visualized as a histogram of latent variables, where the x-axis represented the latent dimension and the y-axis the frequency of occurrences (Fig. 1C). Each bin was color-coded using a green-magenta colormap corresponding to different structural patterns in the latent space.

The latent-space histogram enabled spatial mapping of image regions to structural classes. In this representation, magenta corresponded to background regions, including droplet interiors lacking visible bacteria and the surrounding dark area, while green represented bacterial features such as individual cells, aggregates, and larger biofilm formations. The color assignments were determined through visual inspection of representative crops. A threshold along the latent dimension was manually selected to separate background from bacterial regions, guided by a clear visual transition between feature-free and biofilm-rich areas. This threshold was applied consistently across all datasets. Representative crops are arranged by their latent-bin positions, as shown in Fig. 1D. Using this classification, spatial maps of biofilm structures were generated by overlaying the mapped colors onto the original droplet images. This was achieved by passing each image through the trained VAE using a structured grid approach that preserved spatial context. Each grid section was assigned a latent value based on its content, then colorized according to its classification. A stride-based sampling strategy ensured smooth transitions between adjacent areas, minimizing abrupt color shifts and preserving spatial continuity.

This workflow formed the basis for a segmentation pipeline capable of generating consistent masks for isolating and quantifying bacterial structures. These masks were used to extract morphological metrics, including size, area distribution, and spatial organization, providing a quantitative foundation for analyzing biofilm structures within droplet microenvironments.

3. Results and discussion

3.1. Fluorescence microscopy: Antibiotic sensitivity screening

Fluorescence microscopy enables rapid and specific quantification in high-throughput assays, and we used this modality to validate the platform by testing whether it could capture population-level responses to environmental variation. Fluorescence was introduced through genetic modification by incorporating reporter genes that encode fluorescent proteins under the control of specific promoters. In these constructs, the fluorescent protein gene is transcriptionally linked to target genes that are active in particular physiological states, so that when the target gene is expressed, the fluorescent protein is produced simultaneously and emits detectable fluorescence. This approach ensures that fluorescence serves as a proof for the expression of state-specific proteins rather than an independent property of the cell [46].

Commonly used fluorescent reporter genes, such as variants of Green Fluorescent Protein (GFP) [47] or other fluorescent proteins, are genetically encoded and expressed as part of the bacterial protein synthesis machinery. When expressed, these proteins fold into structures that generate a fluorophore, enabling live-cell imaging of gene expression dynamics without the need for external dyes.

In this study, flagellin and endospore coating proteins were selected as markers of distinct life states in the fluorescent *B. subtilis* strain MTC871. Fluorescent protein expression was placed under the control of the corresponding promoters, ensuring that fluorescence in each

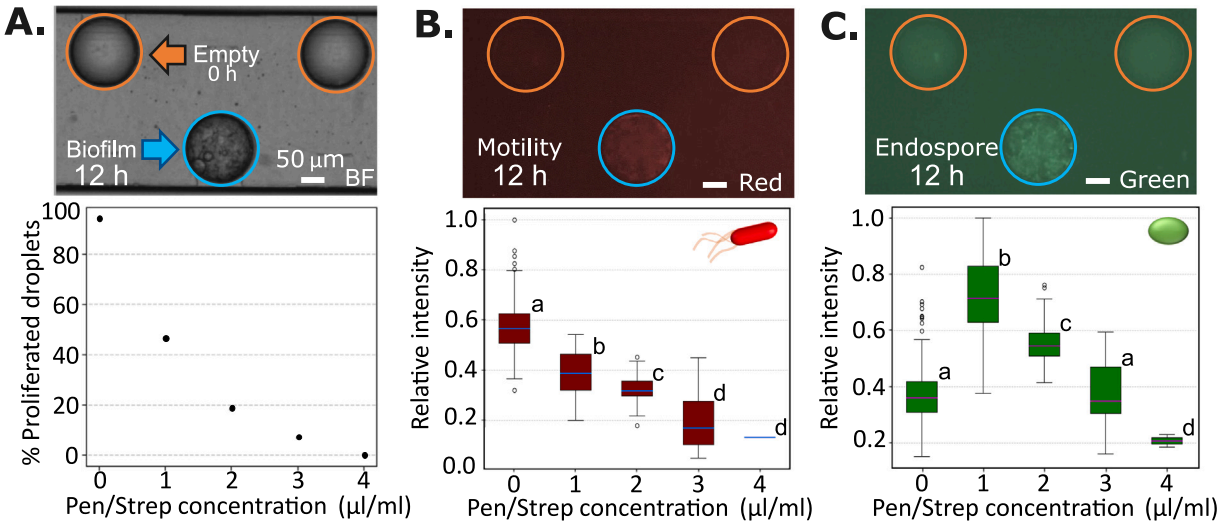

Fig. 2. Biofilm formation in the presence of antibiotics after 12 h of incubation. A. Droplets are considered empty or proliferated, and their proportion depends on the presence of antibiotics in the medium. Increasing antibiotic concentrations reduced the proportion of droplets showing any signs of growth. B. The signal intensity of the red channel indicates the presence of planktonic bacteria. The signal is negligible in empty droplets but varies in proliferated droplets, depending on the presence of antibiotics. The abundance of planktonic bacteria in proliferated droplets was inversely correlated with antibiotic concentration. C. The signal intensity of the green channel indicates the presence of endospores, a consequence of biofilm formation. Empty droplets show a weak signal, while proliferated droplets differ according to antibiotic presence. The highest spore production happened for low concentrations of antibiotic, while in its absence, spore production was comparable to the MIC at 4 µL/mL. Games–Howell post hoc comparisons were performed; concentrations not sharing a common letter differ significantly ($p < 0.05$).

channel is restricted to cells actively expressing these life-state-specific genes and thus enabling discrimination of physiological subpopulations based on their fluorescent profiles.

To evaluate how these subpopulations respond to antibiotic exposure, we quantified proliferation across antibiotic concentrations in a droplet-based high-throughput format. After 12 h — when full population development is expected according to the growth curve of *B. subtilis* (see SI Appendix A, Fig. A.1) — a single fluorescence image was acquired to assess the relative abundance of motile cells and endospores. These two stages were chosen as a reference for population development: motile bacteria constitute the starting population, while spores appear later. Moreover, endospores are highly tolerant to environmental conditions, in contrast to motile bacteria, which remain susceptible to antibiotics even at low concentrations.

Droplets were imaged at 4× magnification to capture multiple droplets per frame, which were then segmented and analyzed individually. Four experiments were performed, consisting of approximately a batch of 500 droplets, 100 droplets for each antibiotic concentration; the specific numbers can be found in SI Appendix G, Table G.2. Consistent fluorescence intensity and exposure settings were maintained across all antibiotic concentrations for both emission channels. Droplets lacking signal in any channel were classified as empty, indicating an absence of bacterial proliferation, in contrast to droplets where growth was observed (see Fig. 2A). For each droplet, the mean fluorescence intensity per channel was calculated and subsequently averaged across all biofilm-positive droplets within the same antibiotic concentration group. The final data were normalized relative to the concentration that exhibited the highest intensity for each channel. Welch's one-way analysis of variance (ANOVA) showed a significant effect of antibiotic concentration on both motility ($F(4, 6.01) = 1405$, $p < 0.001$) and endospore formation ($F(4, 4.53) = 212$, $p < 0.001$) [48–50]. These results are presented in SI Appendix G, Tables G.3–G.4 for motility and Tables G.5–G.6 for endospore formation. Statistical analysis of relative fluorescence intensity across replicates of different antibiotic concentrations was performed using one-way ANOVA. The ANOVA comparing replicates between experiments and concentrations is available in SI Appendix G, Tables G.7–G.8 and G.10–G.11. Replicates within the same concentration were statistically indistinguishable, whereas comparisons between different antibiotic concentrations revealed significant differences (SI Appendix G, Tables G.9 and G.12). A minor exception was observed for endospore fluorescence between 0 and 3 µL/mL, where values were comparable, although motility-associated fluorescence remained significantly different.

The variability observed among droplets within the same treatment group primarily reflects biological heterogeneity in the initial bacterial load per droplet. Unlike single-cell Poisson loading approaches [51], the experimental design intentionally allowed multiple cells per droplet to capture early biofilm formation dynamics. Based on calculations present in the SI Appendix A.2, an average of approximately 14 cells per droplet is expected at the encapsulation time. Variations in cell number and viability at encapsulation contribute to differences in subsequent growth and fluorescence intensity, accounting for the observed dispersion within batches.

Increasing antibiotic concentration led to a decreased number of proliferated droplets within each batch, as shown in Fig. 2A. Given that all droplets were initially populated, the absence of growth indicated that the antibiotic inclusion had eliminated the initially encapsulated CFU. Initially, the bacteria in suspension were motile and therefore more susceptible to antibiotics. Consequently, in droplets where proliferation occurred, the fluorescence signal from motile bacteria decreased with increasing antibiotic concentration (Fig. 2B). Interestingly, at sub-inhibitory concentrations well below the Minimum Inhibitory Concentration (MIC) for Pen/Strep (5 µL/mL), endospore formation was enhanced compared to antibiotic-free conditions (Fig. 2C). The fluorescence intensity in these droplets remained comparable to the antibiotic-free case up to 3 µL/mL, indicating a broad concentration range in which antibiotic exposure paradoxically stimulates development in surviving populations. Beyond this threshold, population survival was significantly impaired. Notably, fluorescence intensity differed between the two fluorophores, precluding direct quantitative comparisons across channels.

The presence of endospore-associated fluorescence reflects the natural developmental cycle of *B. subtilis* biofilms rather than antibiotic-induced stress alone. Sporulation is a well-established response to nutrient limitation and other environmental stressors and does not

require antibiotic exposure [52–54]. In the droplet-based system, nutrients are finite and confined within each microenvironment. As bacterial growth progresses, nutrient depletion and metabolite accumulation create starvation conditions that promote the transition from active growth to dispersal and sporulation [55]. Thus, even in the absence of antibiotics, environmental constraints inherent to the droplet system are sufficient to induce sporulation. While antibiotics can further modulate this stress response [56], their presence is not a prerequisite for endospore formation. These results reflect a response to perceived environmental stress, i.e., antibiotic exposure. Sporulation in *B. subtilis* shares the same regulatory pathway as biofilm formation through Spo0A, where sporulation is mainly triggered by high concentrations reached in a compact community under starvation conditions [57–60]. Consequently, an increased presence of endospores may indicate biofilm formation that allowed more cells to reach this state. Stressors, including antibiotics, are known to trigger bacterial organization and biofilm formation [61,62]. This phenomenon occurs for both the antibiotic used (Pen/Strep; [63–65]) and *B. subtilis*, sometimes due to a direct influence on communication machinery [66] or indirectly by affecting processes such as sliding motility due to colony growth [67]. However, in this case, this antibiotic combination is known not to directly affect sporulation but rather growth [68], so the observed differences in population dynamics can be attributed to environmental stress.

These results underscore the importance of precise antibiotic use, as inappropriate exposure — particularly at low or trace levels — may inadvertently enhance bacterial tolerance by stimulating biofilm formation and/or sporulation. This emphasizes the need to account for biofilm-related parameters — such as the concentration range that promotes biofilm development or the threshold for its onset — when evaluating antibiotic efficacy and associated risks [69,70]. The findings also demonstrate the utility of the platform for studying bacterial population dynamics.

3.2. Validation and performance of the VAE-based segmentation

An important goal of this work is to develop an analysis pipeline that also works for generic, non-genetically modified bacterial strains using bright-field microscopy. Because bright-field images lack a direct reporter signal, their quantification requires more advanced computational approaches. For this reason, we implemented a VAE–based analysis pipeline to extract meaningful structural information from bright-field images, as detailed in the Methods. Before applying the model to large-scale datasets, the VAE-based segmentation was quantitatively validated against independent manual annotations as shown in Fig. 3. The annotated dataset consisted of 91 frames from a single droplet experiment, and all three annotators worked independently on the same images to enable direct comparison of their segmentations. The process required meticulous frame-by-frame inspection and was both time-consuming and challenging, as bacterial structures often appeared heterogeneous with subtle intensity variations, making precise delineation difficult.

Annotators A and B, both experienced in microscopy-based bacterial segmentation, spent approximately 8.5 h and 10.2 h, respectively, completing the task in *Fiji*. Annotator C, who had no prior experience with bacterial imaging but was trained in image analysis, annotated the same dataset, spending approximately 10.3 h on the task using Procreate (Mac OS app). This inclusion was intentional to assess how non-specialist users perform under the same conditions. Due to the increasing complexity of the images over time, annotation effort varied substantially across frames: early-stage images with sparse bacterial presence typically required less than 2 min to analyze, whereas late-stage images with dense, dispersed bacterial regions often took more than 8 min each.

Overall, manual annotation demanded several focused sessions and sustained visual attention, highlighting both the subjectivity and practical limitations of manual segmentation. These challenges underscore the value of unsupervised, automated, and reproducible analysis using the VAE-based framework presented here.

The model's predicted segmentations were compared independently against each manual annotation set as well as a majority-vote consensus mask derived from them. To quantify performance, standard pixel-level metrics were computed based on the four outcomes of binary classification: true positives (TP), false positives (FP), false negatives (FN), and true negatives (TN). Here, TP denotes correctly identified bacterial pixels, FP corresponds to background pixels incorrectly labeled as bacterial, FN represents bacterial pixels missed by the model, and TN refers to correctly classified background pixels.

From these quantities, five complementary performance metrics were derived: Specificity, Recall, Precision, Accuracy, and Dice coefficient. Together, they provide a comprehensive assessment of the model's performance across both bacterial and background regions. Specificity measures the ability to correctly classify background regions as non-bacterial, while Recall (or sensitivity) quantifies the fraction of bacterial pixels correctly detected.

Precision measures the proportion of predicted bacterial pixels that are correct. Accuracy summarizes the overall proportion of correctly classified pixels, and the Dice coefficient quantifies the spatial overlap between predicted and annotations, reflecting the combined influence of Recall and Precision. A summary of these metrics, their corresponding formulas, and interpretations is provided in SI Appendix F, Table F.1, which serves as a reference for the quantitative evaluations presented below.

Quantitative validation results are summarized in Fig. 3. Fig. 3A and Fig. 3B show radar plots showing the mean values of key metrics (Specificity, Recall, Precision, and Accuracy). Fig. 3A displays the pairwise comparisons among annotators (A↔B, A↔C, and B↔C). All pairs demonstrate similar performance across metrics, confirming consistent manual segmentation despite differences in experience.

The B↔C comparison exhibits the highest mean Precision and Accuracy, indicating that Annotator C — although less experienced — produced results closely matching those of Annotator B. This likely reflects the longer time both spent per frame compared to Annotator A, yielding more refined boundaries but reduced practicality for large datasets. In contrast, the A↔C comparison shows a modest decrease in Recall, suggesting slight differences in delineating faint or diffuse bacterial regions.

Nonetheless, the narrow standard deviations observed across all pairs highlight stable inter-annotator agreement. This consistency defines the practical upper limit of achievable segmentation accuracy, as even human experts rarely achieve perfect overlap. Accordingly, inter-annotator agreement serves as the benchmark against which to interpret model performance.

Fig. 3B extends the analysis to model comparisons (Model↔A, Model↔B, Model↔C, and Model↔MV(ABC)). The model's performance falls within the range defined by human annotators, demonstrating segmentation accuracy approaching human-level reliability. Specificity and Accuracy remain consistent, confirming robust background classification. Slightly lower Precision-most notably in comparison with Annotator C-suggests that the model occasionally includes faint or low-contrast regions typically excluded by human annotators. Conversely, Recall values are comparable to or slightly higher than those of the annotators, indicating that the model effectively captures bacterial regions. The comparison with the majority-vote consensus (Model↔MV (ABC)) shows balanced results across metrics, underscoring the consistency of automated segmentation relative to the collective human reference.

This behavior is expected in label-free BF imaging, where early or low-density biofilm is not marked by a dedicated high-contrast reporter but appears as subtle intensity/texture variations that overlap with background heterogeneity. In this regime, acquisition effects such as illumination non-uniformity, mild defocus, and droplet curvature/shading near boundaries can generate patterns that visually resemble weak

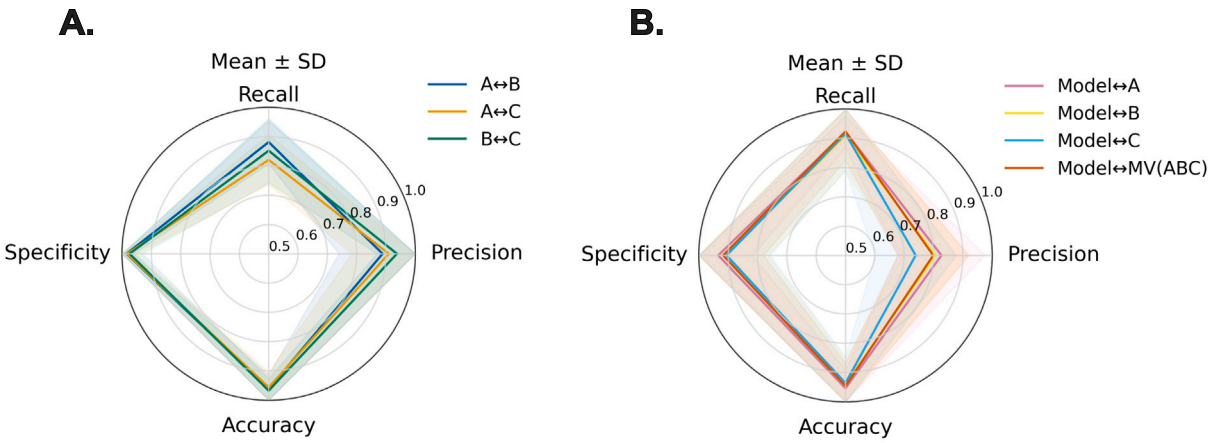

C. Performance Metrics Across Annotator Agreement and Model validation (Mean ± SD)

Comparison	Specificity	Recall	Precision	Accuracy
A↔B	0.985 ± 0.023	0.882 ± 0.074	0.888 ± 0.149	0.961 ± 0.047
A↔C	0.983 ± 0.029	0.821 ± 0.085	0.909 ± 0.126	0.956 ± 0.052
B↔C	0.975 ± 0.043	0.852 ± 0.110	0.937 ± 0.068	0.968 ± 0.041
Model↔A	0.934 ± 0.116	0.922 ± 0.054	0.827 ± 0.148	0.954 ± 0.062
Model↔B	0.910 ± 0.148	0.909 ± 0.121	0.806 ± 0.112	0.940 ± 0.086
Model↔C	0.906 ± 0.149	0.916 ± 0.124	0.739 ± 0.139	0.936 ± 0.088
Model↔MV(ABC)	0.917 ± 0.138	0.924 ± 0.100	0.799 ± 0.122	0.946 ± 0.077

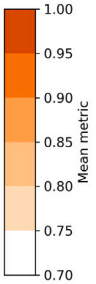

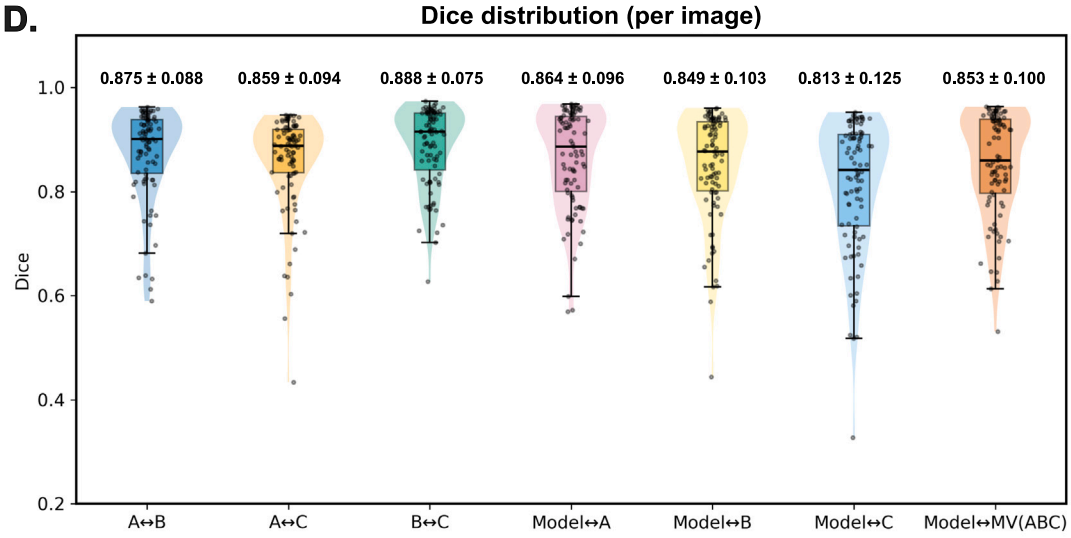

Fig. 3. Quantitative validation across annotators and the VAE model. A. Radar plot of inter-annotator agreement. B. Radar plots comparing model predictions with each annotator and with the majority-vote consensus. C. Heat-map table of mean ± SD performance metrics across all comparisons, where color intensity encodes the mean metric value (see color bar) to facilitate visual comparison across annotator pairs and model validations. D. Per-image Dice distributions showing consistent inter-annotator overlap and comparable model performance relative to human annotations.

biofilm signal, making the distinction intrinsically ambiguous even for human annotators. From an algorithmic perspective, our segmentation is derived from a latent-space-driven pseudo-color reconstruction and converted into a binary mask by thresholding the latent-derived output. In low-contrast regions, many pixels lie close to the decision boundary between background and faint bacterial borders; small photometric or texture variations can shift these borderline pixels across the threshold, leading to small false-positive regions and a corresponding decrease in precision. This effect is amplified when true biofilm coverage is low, since a small number of additional pixels can disproportionately impact precision-based metrics, consistent with the error patterns observed in Fig. 4.

Fig. 3C summarizes these outcomes as mean ± standard deviation values for each metric and comparison. For improved interpretability, this summary is presented as a heat-map styled table in which color intensity encodes the mean metric value (see color bar; darker shades indicate higher values). This format enables rapid visual comparison across annotator ↔ annotator and model ↔ annotator evaluations while retaining the exact numerical values in each cell. Consistent with this heat-map overview, the model's averages align closely with

those of experienced annotators, and the small deviations observed in both human and model comparisons indicate stable and reproducible performance across the dataset. Fig. 3D presents the per-image distribution of Dice coefficients for all pairwise comparisons. Unlike the mean ± SD summary in Fig. 3C, these distributions reveal frame-to-frame variability. The Dice coefficient was chosen because it directly quantifies spatial overlap between two segmentations, providing an interpretable measure that integrates both Recall and Precision. Inter-annotator Dice values (A↔B, A↔C, and B↔C) remain consistently high (typically above 0.85), confirming strong manual agreement. Model–annotator comparisons show slightly lower central values but narrow distributions, indicating reproducible performance. The Dice value between the model and the majority-vote consensus (Model↔MV(ABC)) lies within the same range as inter-annotator values, demonstrating that the model captures bacterial structures with human-level accuracy while achieving full automation.

To complement the quantitative analysis, qualitative overlays are shown in Fig. 4. Each panel compares the model predictions with the manual annotations: Model↔Annotator A (second row), Model↔Annotator B (third row), and Model↔Annotator C (fourth row). For each case, the raw grayscale image is displayed alongside the segmentation contours. Pixel-wise overlays visualize true positives (TP, correctly segmented bacterial regions, cyan), false positives (FP, model-predicted regions absent in the annotation, yellow), and false negatives (FN, annotated regions missed by the model, violet). Dice scores are shown below each corresponding example.

A clear trend emerges in Fig. 4: Dice values decrease gradually from top to bottom. The highest-scoring cases correspond to images with well-defined bacterial regions exhibiting sharp boundaries and strong contrast, leading to high agreement between model and annotators. Mid-range examples contain irregular or heterogeneous features, where faint edges and dispersed biofilm lead to ambiguity and discrepancies between annotations and predictions. The lowest-scoring examples are characterized by sparse, weakly defined bacterial structures, posing a significant challenge for segmentation. When bacterial coverage is minimal, small deviations in predicted area yield large relative Dice differences, since the metric is highly sensitive to pixel mismatches in small regions. These observations indicate that Dice reductions primarily reflect structural ambiguity and bacterial sparsity rather than systematic model errors.

Bright-field (BF) imaging is inherently sensitive to acquisition-dependent variability (e.g., illumination/exposure differences), which can manifest as changes in global brightness and contrast across experiments or imaging sessions. To evaluate the robustness of the VAE-based segmentation to such photometric variability, a controlled analysis was performed on the original BF dataset by applying three deterministic brightness (B)/contrast (C) transformations that remain within the practical dynamic range of the raw 8-bit images. The corresponding pixel-intensity histograms (log-count scale) are shown in SI Appendix H, Fig. H.9, where the histogram of the raw dataset provides the baseline intensity distribution and the perturbed cases illustrate realistic shifts consistent with common acquisition variability.

Specifically, Case 1 (C+10, B+10) induces a moderate right-shift and redistribution toward higher intensities, consistent with mildly increased illumination/exposure. Case 2 (C−15, B−5) shifts the distribution toward lower intensities and compresses contrast, emulating a slightly under-exposed or lower-contrast acquisition. Case 3 (C+15, B+15) produces a stronger (but still plausible) increase in brightness and contrast, representative of higher-exposure or higher-contrast conditions. These parameters were selected to reflect feasible acquisition-to-acquisition variability, rather than extreme distortions that could misrepresent the imaging conditions.

We assessed robustness to brightness/contrast variability by applying three deterministic photometric perturbations to the original BF images and re-running the trained model without retraining. Model ↔ Annotator A agreement remained stable at both the example level (SI Fig. H.10A) and the dataset level (SI Fig. H.10B; mean ± SD Specificity/Recall/Precision/Accuracy), consistent with the overall validation result that model performance falls within the inter-annotator range.

Taken together, these validation and robustness results indicate that the proposed unsupervised segmentation is not only human-comparable on the annotated benchmark, but also resilient to realistic acquisition variability encountered in label-free BF microscopy.

In previously reported bacterial and biofilm segmentation studies [28–33], supervised and semi-supervised deep-learning approaches typically achieve Dice values in the range of 0.75 to 0.90. In comparison, our unsupervised VAE-based method achieves comparable performance, with Dice coefficients typically exceeding 0.80 and reaching around 0.85 against the majority-vote reference, using only two real microscopy images for training and without the need for pixel-level annotations. This demonstrates that accurate human-comparable bacterial segmentation can be achieved without any pixel-level ground truth.

3.3. Quantitative analysis of biofilm development and structural evolution in droplets

With the population-level fluorescence assays and VAE-validated bright-field segmentation in place, we proceeded to quantify biofilm development and structural evolution in droplets using bright-field time-lapse imaging. Due to the constraints of the imaging system, this required a trade-off between droplet generation throughput and temporal resolution. The imaging interval was adjusted according to experimental priorities: higher droplet counts increased statistical power but necessitated longer acquisition intervals, whereas shorter intervals provided finer temporal detail on biofilm life-cycle progression. Accordingly, a throughput-optimized setting was used for substance-effect screening, while high-resolution imaging was prioritized for detailed analysis of structural transitions within the biofilm life cycle.

A 17.5 h time-lapse sequence comprising 165 images (Fig. 5A) was processed using the trained VAE together with the structured grid approach. This generated latent-space feature representations and enabled the generation of overlay images (Fig. 5B), in which green indicates bacterial structures and biofilms, while magenta denotes the droplet background, providing clear visual separation between bacterial regions and the surrounding medium. From these overlays, the green masks were used to quantify bacterial coverage within droplets (Fig. 5C). To enable reproducible quantitative analysis, we adopted an operational segmentation-first framework, dividing segmented regions by projected pixel area into three classes: aggregates, biofilm-like clusters, and internal patches.

Motile, free-swimming bacteria initially formed clusters, distributed throughout the droplet, which we refer to as aggregates. These structures grew over time, gradually losing motility and transitioning into biofilms. Instances of the motility of these aggregates can be found in SI Video 3. Biofilm identification was based not only on size but also on the persistence of motility and adhesion to the droplet interface [71–73], which could be assessed directly through BF microscopy. This interpretation follows the current consensus that biofilm formation is a biological process rather than a purely morphological transition [74–77]. In confined microfluidic droplets, where attachment to solid interfaces is limited, such biofilm-like behavior can still arise through matrix production and collective immobilization of cells, distinguishing these structures from transient aggregates or clumps [78]. For classification, aggregates — outlined in yellow — were defined as bacterial clusters between 300 and 4999 pixels^2 (3.32–55.4 μm^2), while clusters with an area equal to or greater than 5000 pixels^2 (approximately 55.4 μm^2) were classified as biofilm—outlined in blue). These biofilm structures lay on the bottom of the droplet and often expanded to cover much of the droplet's bottom surface, although growth was not always uniform. Over time, regions with reduced bacterial density

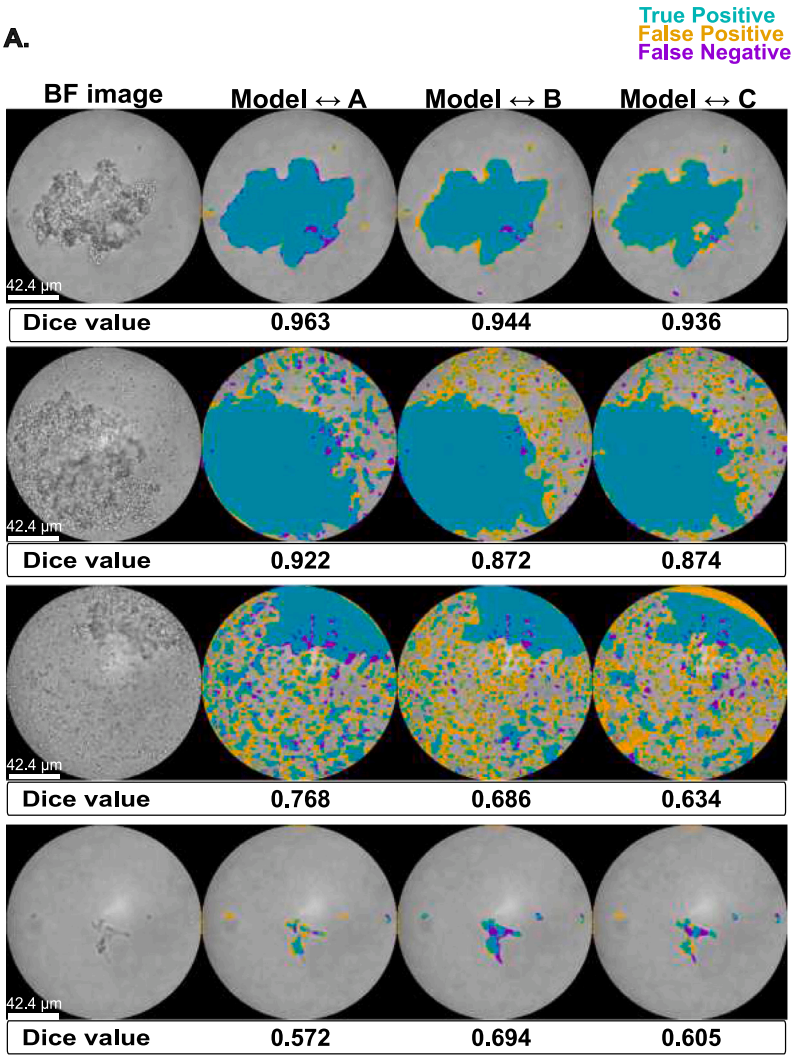

Fig. 4. Representative pixel-wise overlays comparing model-generated and manually annotated biofilm segmentations. A. Each row shows the BF image with the model prediction compared against each annotator (A–C). Pixel-wise overlays indicate true positives (TP; correctly segmented bacterial pixels), false positives (FP; predicted by the model but absent in the annotation), and false negatives (FN; present in the annotation but missed by the model), as defined in the legend. Corresponding Dice values are reported to link visual differences to quantitative metrics.

— termed patches and outlined in orange — emerged within the biofilm. Holes in the biofilm can nucleate at local weaknesses within the biofilm matrix and subsequently expand through either mechanical disruption or enzymatic degradation of structural components such as extracellular DNA and matrix proteins [79–81]. These processes have been directly observed in microfluidic and pellicle biofilms, where matrix heterogeneity and age-dependent cohesion create preferential sites for detachment [79]. In *B. subtilis*, temporally heterogeneous matrix production, protease activity, and calcium-mediated weakening of the matrix have been implicated in both active and passive dispersal from the pellicle, leading to cell release and visible hole formation [82–84]. In this study, we defined patches as holes within the biofilm only if their area exceeded 500 pixels^2 (5.54 µm^2) and localized within a biofilm, distinguishing low-density areas from cohesive biofilm. Very small regions below 300 pixels^2 (less than 3.32 µm^2) were considered negligible and excluded from the analysis. These ranges were chosen to exclude noise and single cells while capturing multicellular clusters of increasing size, but we emphasize that these thresholds represent operational criteria rather than strict biological boundaries.

Our approach followed a logic similar to previous segmentation-based analyses: in *B. subtilis* imaging, pixel-level segmentation was converted into distributions to characterize cellular organization [85], while size and spatial partitioning were used to distinguish core and peripheral regions within macrocolonies [86]. Likewise, tools such as BiofilmQ apply size- and region-based segmentation as the foundation for biofilm quantification in 3D [87].

In our case, we adapted this segmentation-first logic to the droplet microfluidics context, where thresholds provide a practical means to track the emergence and structural dynamics of bacterial clusters across thousands of droplets in parallel. We note that our analysis does not directly assess extracellular matrix production or adhesion to the droplet interface, and these criteria were therefore not part of our classification. Instead, the thresholds provide an operational framework for distinguishing structures of different sizes within the image data. Accordingly, we interpret the categories of aggregates, biofilm, and patches as structural classes defined for quantitative image analysis, rather than as canonical developmental stages of *B. subtilis* biofilms.

Having established this classification framework, we next used it to follow the temporal dynamics of bacterial communities within droplets. After 7.5 h, a dispersal phase became evident [82,88–90], characterized by cell detachment from cohesive clusters and the gradual breakup of biofilm-like regions. At later stages, droplets contained a heterogeneous mixture of biofilm remnants, smaller aggregates, patches, and residual debris. This complexity made it increasingly difficult to separate intact

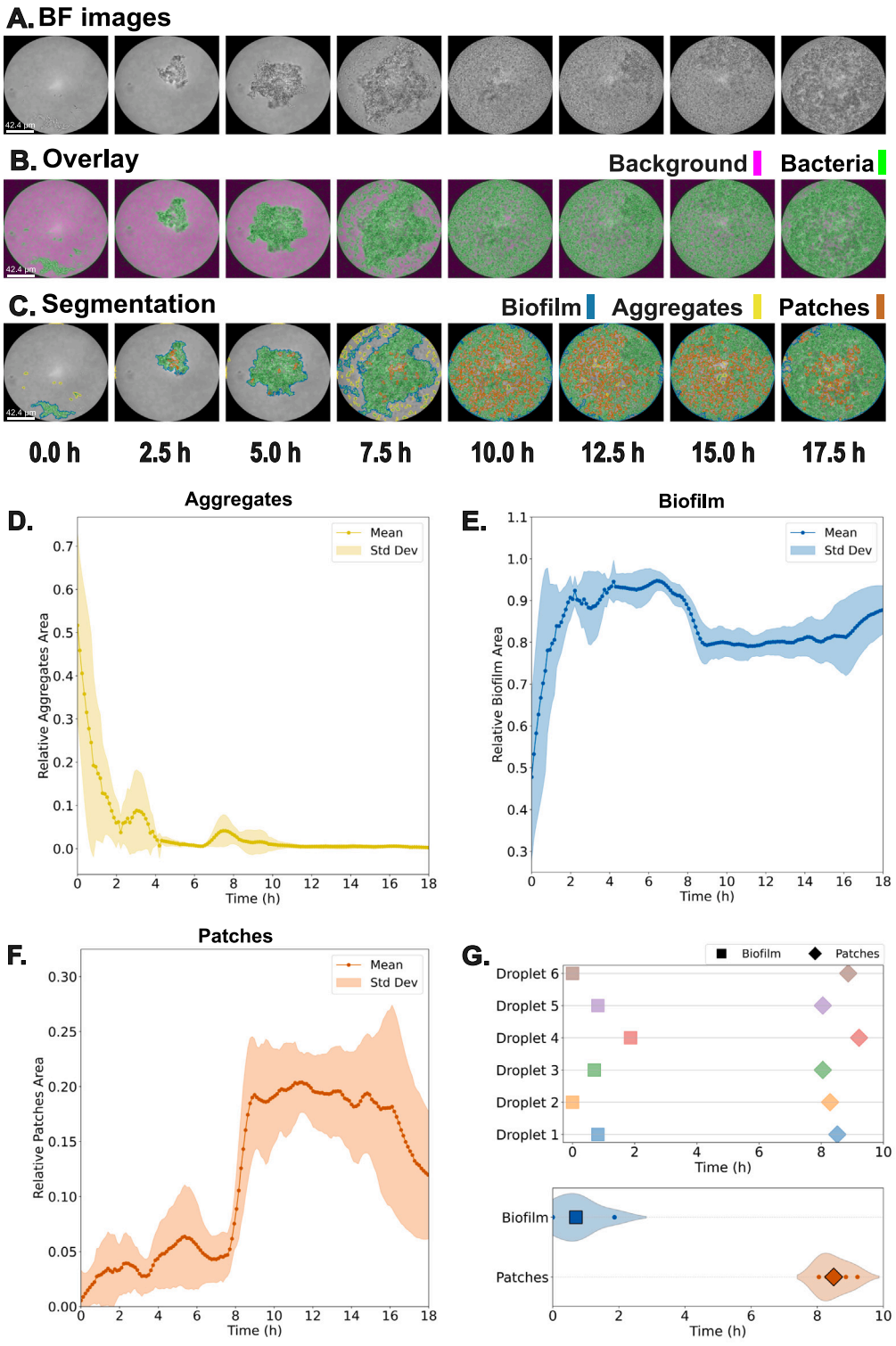

Fig. 5. Spatiotemporal analysis of biofilm formation. A. Bright-field time-lapse images show biofilm growth over 17.5 h. B. Overlay images derived from latent space distribution; green areas denote bacterial presence. C. Structural segmentation highlighting spatial distribution: biofilm regions outlined in blue, aggregates in yellow, and patches in orange. D. Relative area of aggregates over time, where the sharp decrease coincides with initial stages of biofilm formation. E. Temporal changes in relative biofilm area, showing a steep increase and decrease corresponding to formation and dispersal. F. Relative area of patches, capturing the emergence of openings within the biofilms surface. G. Top: Mean of the positive maximum rate of change for biofilm and patches, summarizing their structural evolution. Bottom: violin plot of the distribution of maximum growth rate for biofilm and patches across six droplets, illustrating variability in their expansion and dispersal. Central symbols indicate mean values.

biofilm from disintegrating fragments, indicating a shift toward a more dispersed state. To quantify this progression, we measured the area occupied by each structural category relative to the total bacteria-containing area at each time point, providing insight into the processes of biofilm formation, maturation, and dispersal.

Fig. 5D illustrates the presence of aggregates, the predominant structures observed during the early stages of the experiment. These aggregates originated from the initial suspension of free-swimming bacteria. Over the first 2 h, the relative area occupied by these structures gradually decreased as they progressively merged into larger clusters. Due to the predefined aggregate area threshold, these larger structures were classified as biofilm. As the remaining motile aggregates increased in size, bacterial motility diminished, causing the aggregates to settle at the base of the droplet (in the imaging focal plane), leading to a temporary increase in aggregate detection between 2 and 4 h. This was followed by their integration into biofilms, resulting in a sustained low aggregate ratio until the 7.5 h. At this point, a second peak in aggregate presence occurred, triggered by the rapid escape of bacteria during biofilm dispersal. After approximately 2 h, the aggregate ratio dropped again and remained negligible for the rest of the experiment.

Initially, biofilms formed through the merging of aggregates and exhibited rapid growth, as shown in Fig. 5E. Over time, biofilms became the dominant structure within the droplet. Although biofilm growth continued steadily through bacterial division, the relative ratios remained stable until the onset of dispersal. An exception to this stability occurred with the sudden appearance of patches caused by the extension of elongated structures that reattached to the biofilm at another point, forming loops. These loops temporarily increased the patch area but were eventually filled in as bacterial division progressed. Once dispersal began, the biofilm ratio declined significantly while the presence of aggregates and patches increased. Following dispersal, some biofilm clusters persisted as stable, coherent structures. A few of these appeared to grow further [90,91], as reflected by the rise in biofilm ratio during the final 2 h. These appeared as darker regions at the bottom of the droplet that maintained their shape while growing into bigger structures. This phenomenon could be hypothesized to be another biofilm formation cycle after dispersal, where endospores are produced due to nutritional depletion and the recycling of biofilm remnants. Such secondary biofilm cycle after dispersal has been described in other bacteria like *Pseudomonas aeruginosa* [92]. In *B. subtilis*, both starvation-induced cannibalistic behaviors that redistribute nutrients [93–95] and a connection between biofilm dispersal and spore release have been reported [90]. The combination of these processes could explain the observed repeated biofilm formation after the release of cells and spores indicated by the presence of patches. This correlates with the established relationship between biofilm formation-dispersal and nutrient availability [96–100] and their role in sporulation [82,89]. However, determining whether these secondary structures represent true biofilms or merely accumulating debris would require additional analyses to clarify their chemical and cellular composition.

Patch evolution is shown in Fig. 5F. Patches emerged at times during early aggregation as a consequence of cell orientation. During growth, *B. subtilis* cells often remain attached after division, forming chains that can loop and occasionally reconnect—a common behavior known from biofilm and pellicles [71,85,101–104]. In our droplets, similar chains appeared, most prominently at 3 h 20 min (Fig. 6A), where loop closure transiently increased patch area and produced the first local maximum. Variability in loop formation and chain length contributed to the elevated standard deviation. As loops filled in, the patch ratio declined until dispersal triggered a sharp, sustained rise, reflecting structural breakdown across droplets. Although consistent with known chaining behavior, confinement may modulate its frequency or geometry.

SI Video 4 presents the *z*-stack data across time, confirming that the biofilm remained in the same focal plane throughout the entire observation period, thereby validating the stability of the analyzed structures. In several droplets, as shown in Video 3, multiple small aggregates — each composed of more than one cell — were initially observed. In all recorded cases, these aggregates gradually merged into larger, coherent structures. This merging likely arose either from the attainment of a critical size that restricts motility or from the differentiation of a substantial fraction of the population into a sessile state.

Conversely, dispersal events were characterized by an increase in the number of freely swimming cells, as shown at the end of SI Video 4. During this phase, cells were no longer permanently attached to the droplet interface but moved independently throughout the droplet volume. These transitions — from motile aggregates to sessile biofilms and subsequently to dispersed states — represent clear, biologically driven processes observable across the three defined developmental stages.

The dynamics of aggregates, biofilm, and patches collectively offered a comprehensive view of biofilm lifecycle events in nutrient-limited spaces. Two key transitions were identified: the biofilm formation trigger, defined as the point of maximum growth rate of the biofilm (i.e., the peak of the derivative of the biofilm area curve), and the dispersal trigger, defined as the point of maximum growth rate of patch formation. To capture the variability across droplets, we analyzed the timing and distribution of these transitions in all samples. Fig. 5G displays six recorded droplets, showing the temporal evolution of biofilm structures. Squares and diamonds indicate the time points of peak positive growth for biofilm and patches, respectively, as determined by the derivatives of their relative area ratio curves. Violin plots reveal the distribution of these events, highlighting variability and trends in biofilm and patch formation across the different droplets.

These findings, supported by the unsupervised model that generates feature-based overlays, offer a data-driven perspective on bacterial dynamics within droplets. The minimal training required demonstrates the robustness of the VAE in generalizing structural representations from only two distinctly different microscopy images. The model segmented bacterial regions from the droplet background, which were then operationally classified into aggregates, biofilm-like clusters, or patches based on size thresholds. This two-step workflow revealed a dynamic cycle of growth and dispersal, evidenced by sequential peaks in their area ratios. This approach not only aligns with visual observations but also underscores the potential of unsupervised approaches for reliable, high-throughput analysis of complex biological structures, as further demonstrated in the following section.

3.4. Quantitative analysis of biofilm modifiers

After establishing a baseline for analyzing biofilm dynamics from bright-field time-lapse microscopy images, we applied the workflow to a relevant case study: assessing the impact of biofilm-modifying substances. For this experiment, three types of droplets were generated within the same microfluidic chip: (i) sterile Lysogeny Broth medium serving as a contamination control, (ii) inoculated Lysogeny Broth medium as a negative control, and (iii) inoculated Lysogeny Broth medium supplemented with 1% (v/v) glycerol as the biofilm-promoting agent for *B. subtilis*, making it an ideal candidate to validate the analysis pipeline. Images of the bacterial populations within droplets were acquired and analyzed based on the presence or absence of glycerol. In this case, the focus was on throughput rather than temporal resolution. Accordingly, batches of over 50 droplets per condition were imaged at 40 min intervals over an 8 h observation period, covering the full biofilm development cycle until dispersal begins. After dispersal, potential biofilm segmentation became increasingly challenging for the current model due to the presence of swimming bacteria and debris, so we focused exclusively on the formation process. The resulting images were processed using the previously described unsupervised model.

Sterile Lysogeny Broth droplets showed no signs of bacterial proliferation, confirming the absence of contamination and validating the platform's reliability. Qualitative analysis revealed that droplets

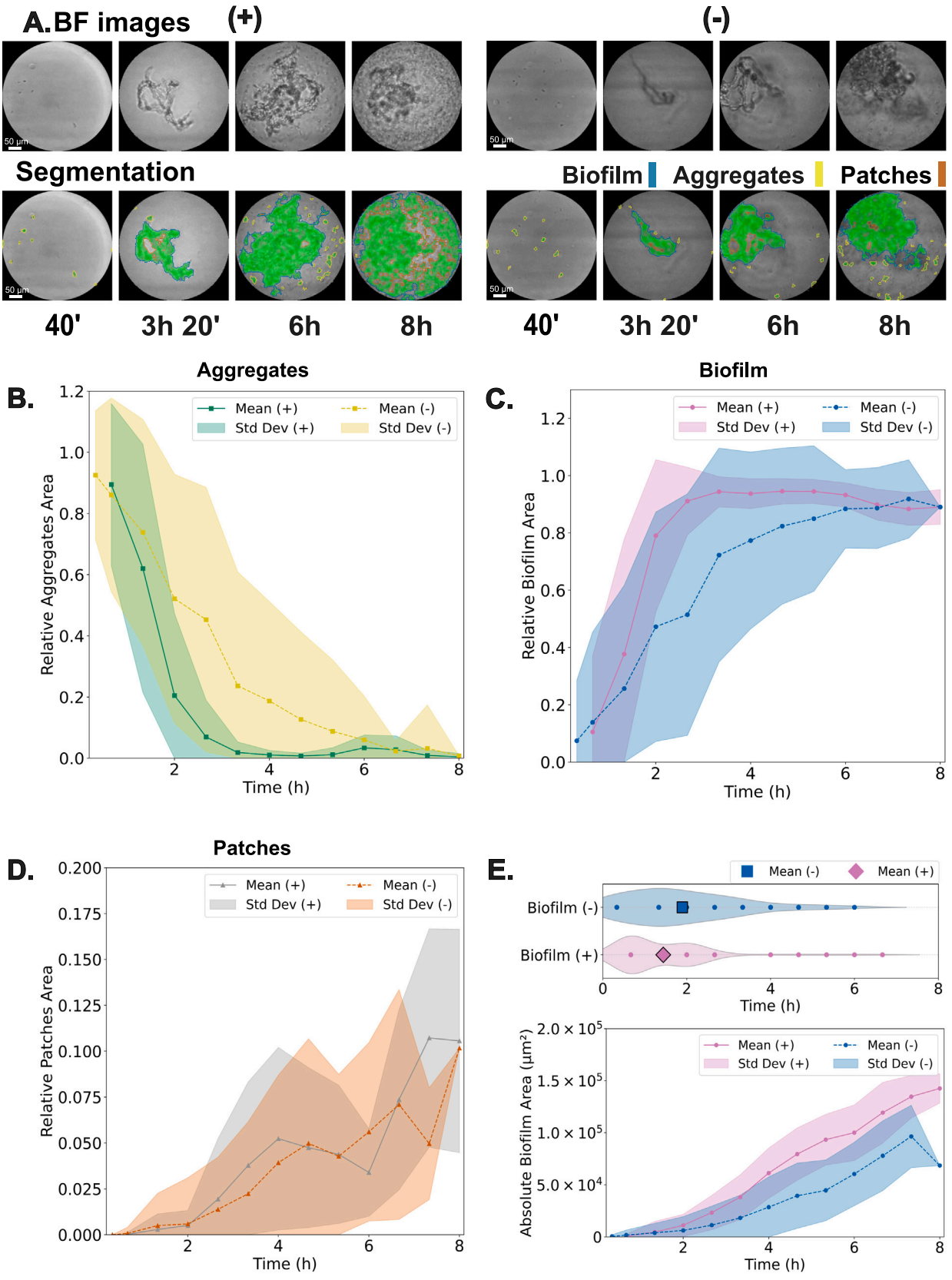

Fig. 6. Influence of glycerol on biofilm formation A. Representative images of biofilm formation at 40 min, 3 h, 20 min, 6 h, and 8 h, under conditions with (+) and without (−) glycerol. B. Relative aggregate area, showing the evolution of aggregates with and without glycerol. C. Relative biofilm area over time, illustrating differences in biofilm growth dynamics between the two conditions. D. Relative patch area, indicating the formation of patches within the biofilm structure under both conditions. E. Violin plot of maximum biofilm growth rate across multiple droplets, illustrating the distribution of growth dynamics under both conditions. This quantitative analysis provides insights into biofilm formation's temporal evolution and glycerol's influence on its structural development.

containing glycerol exhibited faster biofilm formation and showed early signs of dispersal as soon as 6 h into the experiment Fig. 6A. In *B. subtilis*, glycerol is a common component of biofilm-inducing media such as MSgg, where it serves as a carbon source that, in combination with other nutrients and ions (e.g., manganese), promotes matrix production and biofilm formation [101,105]. Previous studies have shown that glycerol, particularly when combined with manganese, enhances matrix production and biofilm formation in *B. subtilis* [105]. Here, we tested glycerol alone, which proved sufficient to induce measurable biofilm responses under our droplet conditions. Quantitatively, the most notable distinction emerged in the statistical distribution of the data. Droplets containing glycerol exhibited a narrower distribution and lower variability, suggesting that glycerol may act more as a signaling molecule than as supplementary nutrition. Specifically, aggregate formation occurred over a shorter time window in the presence of glycerol, and a local maximum in the ratio appeared at 6 h—likely marking the onset of dispersal (Fig. 6B). In contrast, droplets without glycerol only showed a mild increase in aggregate ratio after 7 h. The biofilm ratio (Fig. 6C) followed a similar trend. In droplets with glycerol, biofilms formed more rapidly and reached a stable level within 3 h. In the absence of glycerol, a plateau was only reached after 4 h, consistent with the control data from the previous result section. Patches formation (Fig. 6D) followed a comparable progression in both conditions up to 6 h. While glycerol appeared to slightly accelerate early development, it did not significantly affect the formation of the looped structures that define patches at this stage. However, after 6 h, droplets with glycerol showed a sharp increase in the patch ratio — signaling active dispersal — while droplets without glycerol exhibited this pattern only at the final time point. As a summary metric, the maximum rate of biofilm formation (i.e., the point of fastest biofilm growth) was calculated for both conditions and shown in Fig. 6E. This metric reflects the overall trends in the time series: glycerol induced earlier and more synchronized biofilm formation, while in its absence, the process was slower and more variable.

An absolute representation of biofilm area over time further supported these findings, showing that droplets with glycerol consistently reached larger biofilm-covered areas. Interestingly, although the absolute standard deviation of biofilm sizes was similar between both conditions, their relative variability (as seen in the ratio-based analysis) differed. This highlights the importance of normalized, comparative metrics in identifying patterns within inherently variable biological systems. Moreover, it reinforces the idea that glycerol influences not only biofilm mass but also bacterial organization. Overall, these results validate the platform's effectiveness in quantifying the influence of biofilm modifiers and demonstrate the potential to uncover new insights into the mechanisms driving biofilm regulation.

4. Conclusions

We have developed a robust, versatile platform for both qualitative and quantitative studies of bacterial structures within microfluidic droplets. The platform has been successfully applied to multiple use cases, including antibiotic-sensitivity screening, exploration of biofilm life-cycle dynamics, and evaluation of a biofilm-promoting substance. Its flexibility has been demonstrated across different imaging modalities, analytical workflows, and degrees of automation.

A core strength of the platform lies in its integration of an unsupervised model for automated segmentation and quantification. Using a VAE, high-dimensional image data is encoded into a one-dimensional latent space that preserves essential structural information. The model's performance was validated against multiple human annotators, achieving Dice coefficients comparable to inter-annotator agreement, thereby confirming that automated segmentations reach human-level accuracy. This validation ensures that subsequent quantitative analyzes — such as identifying morphological changes or classifying structural states — are grounded in reliable segmentation performance. Together, these results establish a powerful framework for longitudinal studies, enabling consistent and precise monitoring of biofilm formation and structural transitions over time.

The VAE-based segmentation provides automated identification of bacterial regions across the dataset, generating consistent masks that capture the structural organization within droplets. These segmentation outputs are subsequently processed through a size-based thresholding framework to distinguish smaller aggregates, larger biofilm-like clusters, and internal low-density patches. Analyzing the relative area of these categories over time reveals sequential transitions corresponding to growth, maturation, and dispersal phases. This quantitative approach offers a reproducible means to study structural evolution within confined microenvironments, providing new insights into how bacterial communities reorganize and disperse over time. A remaining limitation is reduced precision in the faintest/lowest-contrast regime of BF images, where intrinsic ambiguity and thresholding of the latent-derived reconstruction can introduce small false-positive regions; addressing this regime is a natural direction for future improvements (e.g., uncertainty-aware outputs or adaptive decision thresholds). Overall, incorporating VAEs into the analysis pipeline significantly enhances our ability to study bacterial structures in detail while greatly reducing the time and labor typically associated with manual annotation or (semi-)supervised model development. Combined with the versatile droplet-based microfluidic system and adaptable imaging and analysis options, this platform offers a comprehensive, scalable solution for future investigations into biofilm formation, growth, dispersal, and regrowth.

CRediT authorship contribution statement

Daniela Pérez Guerrero: Writing – review & editing, Writing – original draft, Visualization, Validation, Software, Methodology, Funding acquisition, Formal analysis, Data curation, Conceptualization. **Jesús Manuel Antúnez Domínguez:** Writing – review & editing, Writing – original draft, Visualization, Methodology, Investigation, Funding acquisition, Data curation, Conceptualization. **Aurélie Vigne:** Writing – review & editing, Supervision, Resources, Project administration, Conceptualization. **Daniel Midtvedt:** Writing – review & editing, Software, Methodology. **Wylie W. Ahmed:** Writing – review & editing, Supervision, Software, Methodology, Conceptualization. **Lisa D. Muiznieks:** Writing – review & editing, Supervision, Resources, Project administration, Conceptualization. **Giovanni Volpe:** Writing – review & editing, Supervision, Software, Methodology, Funding acquisition, Conceptualization. **Caroline Beck Adiels:** Writing – review & editing, Visualization, Supervision, Resources, Project administration, Methodology, Conceptualization, Software, Funding acquisition.

Declaration of Generative AI and AI-assisted technologies in the writing process

During the preparation of this work, the author(s) used ChatGPT in order to improve grammar, clarify wording, and refine the structure of several paragraphs. After using this tool/service, the author(s) reviewed and edited the content as needed and take(s) full responsibility for the content of the published article.

Funding and acknowledgments

This project received support from the European Union's Horizon 2020 research and innovation programme within the Active Matter ITN (grant No. 812780), the Swedish Research Council (grant No. 2019-05401), the Horizon Europe ERC Consolidator Grant MAPEI (grant No. 101001267), and the Knut and Alice Wallenberg Foundation, Sweden (grant No 2019.0079). Jesus Manuel Antúnez Domínguez thanks the Adlerbertska forskningsstiftelsen program from 2023 and 2024. Wylie

W. Ahmed was partially supported by ANR Grant No. ANR-23-CPJ1-0170-01. Thanks also to Dr. Matthew Cabeen, Assistant Professor in the Department of Microbiology and Molecular Genetics of Oklahoma State University, who kindly provided the strain of *Bacillus subtilis* used in this project. And lastly, thanks to Ester Beck Adiels for manual annotation assistance.

Declaration of competing interest

The authors declare that they have no known competing financial interests or personal relationships that could have appeared to influence the work reported in this paper.

Appendix A. Supplementary data

Supplementary material related to this article can be found online at https://doi.org/10.1016/j.microc.2026.117685.

Data availability

Data will be made available on request.

References

[1] R. Popat, D.M. Cornforth, L. McNally, S.P. Brown, Collective sensing and collective responses in quorum-sensing bacteria, J. R. Soc. Interface 12 (2015) 20140882, http://dx.doi.org/10.1098/rsif.2014.0882, URL https://royalsocietypublishing.org/doi/10.1098/rsif.2014.0882.

[2] J.G. Mitchell, K. Kogure, Bacterial motility: links to the environment and a driving force for microbial physics., FEMS Microbiol. Ecol. 55 (2006) 3–16, http://dx.doi.org/10.1111/j.1574-6941.2005.00003.x, URL http://www.ncbi.nlm.nih.gov/pubmed/16420610.

[3] N. Wadhwa, H.C. Berg, Bacterial motility: machinery and mechanisms., Nat. Rev. Microbiol. 20 (2022) 161–173, http://dx.doi.org/10.1038/s41579-021-00626-4, URL http://www.ncbi.nlm.nih.gov/pubmed/34548639.

[4] M.B. Miller, B.L. Bassler, Quorum sensing in bacteria, Annu. Rev. Microbiol. 55 (2001) 165–199, http://dx.doi.org/10.1146/annurev.micro.55.1.165, URL https://www.annualreviews.org/doi/10.1146/annurev.micro.55.1.165.

[5] M.R. Parsek, E. Greenberg, Sociomicrobiology: the connections between quorum sensing and biofilms, TIM 13 (2005) 27–33, http://dx.doi.org/10.1016/j.tim.2004.11.007, URL https://linkinghub.elsevier.com/retrieve/pii/S0966842X04002616.

[6] S. Arnaouteli, N.C. Bamford, N.R. Stanley-Wall, Á.T. Kovács, Bacillus subtilis biofilm formation and social interactions, Nat. Rev. Microbiol. 19 (2021) 600–614, http://dx.doi.org/10.1038/s41579-021-00540-9, URL https://www.nature.com/articles/s41579-021-00540-9.

[7] B.R. Wucher, M. Elsayed, J.S. Adelman, D.E. Kadouri, C.D. Nadell, Bacterial predation transforms the landscape and community assembly of biofilms, Curr. Biology 31 (2021) 2643–2651.e3, http://dx.doi.org/10.1016/j.cub.2021.03.036.

[8] P. Espinal, S. Martí, J. Vila, Effect of biofilm formation on the survival of Acinetobacter baumannii on dry surfaces, J. Hosp. Infect. 80 (2012) 56–60, http://dx.doi.org/10.1016/j.jhin.2011.08.013, URL https://linkinghub.elsevier.com/retrieve/pii/S0195670111003458.

[9] S. Hathroubi, M.A. Mekni, P. Domenico, D. Nguyen, M. Jacques, Biofilms: Microbial shelters against antibiotics, Microb. Drug Resist. 23 (2017) 147–156, http://dx.doi.org/10.1089/mdr.2016.0087, URL http://www.liebertpub.com/doi/10.1089/mdr.2016.0087.

[10] J. Pérez, F.J. Contreras-Moreno, F.J. Marcos-Torres, A. Moraleda-Muñoz, J. Muñoz-Dorado, The antibiotic crisis: How bacterial predators can help, Comput. Struct. Biotechnol. J. 18 (2020) 2547–2555, http://dx.doi.org/10.1016/j.csbj.2020.09.010, URL https://linkinghub.elsevier.com/retrieve/pii/S2001037020303949.

[11] D. Sun, K. Jeannot, Y. Xiao, C.W. Knapp, Editorial: Horizontal gene transfer mediated bacterial antibiotic resistance, Front. Microbiol. 10 (2019) http://dx.doi.org/10.3389/fmicb.2019.01933, URL https://www.frontiersin.org/article/10.3389/fmicb.2019.01933/full.

[12] M. Kolpen, K.N. Kragh, J.B. Enciso, D. Faurholt-Jepsen, B. Lindegaard, G.B. k Egelund, A.V. Jensen, P. Ravn, I.H.M. Mathiesen, A.G. Gheorge, F.B. Hertz, T. Qvist, M. Whiteley, P.Ø. Jensen, T. Bjarnsholt, Bacterial biofilms predominate in both acute and chronic human lung infections, Thorax 77 (2022) 1015–1022, http://dx.doi.org/10.1136/thoraxjnl-2021-217576.

[13] J.M. Sonawane, A.K. Rai, M. Sharma, M. Tripathi, R. Prasad, Microbial biofilms: Recent advances and progress in environmental bioremediation, Sci. Total Environ. 824 (2022) http://dx.doi.org/10.1016/j.scitotenv.2022.153843.

[14] C.J. Linton, A. Sherriff, M.R. Millar, Use of a modified robbins device to directly compare the adhesion of Staphylococcus epidermidis RP62A to surfaces, J. Appl. Microbiol. 86 (1999) 194–202, http://dx.doi.org/10.1046/j.1365-2672.1999.00650.x, URL https://academic.oup.com/jambio/article/86/2/194/6720783.

[15] K. Schwartz, R. Stephenson, M. Hernandez, N. Jambang, B. Boles, The use of drip flow and rotating disk reactors for Staphylococcus aureus biofilm analysis, J. Vis. Exp. (2010) http://dx.doi.org/10.3791/2470, URL https://app.jove.com/t/2470.

[16] J. Azeredo, N.F. Azevedo, R. Briandet, N. Cerca, T. Coenye, A.R. Costa, M. Desvaux, G. Di Bonaventura, M. Hébraud, Z. Jaglic, M. Kačániová, S. Knøchel, A. Lourenço, F. Mergulhão, R.L. Meyer, G. Nychas, M. Simões, O. Tresse, C. Sternberg, Critical review on biofilm methods, Crit. Rev. Microbiol. 43 (2017) 313–351, http://dx.doi.org/10.1080/1040841X.2016.1208146, URL https://www.tandfonline.com/doi/full/10.1080/1040841X.2016.1208146.

[17] T.S. Kaminski, O. Scheler, P. Garstecki, Droplet microfluidics for microbiology: techniques, applications and challenges, Lab A Chip 16 (2016) 2168–2187, http://dx.doi.org/10.1039/C6LC00367B, http://dx.doi.org/10.1039/C6LC00367B http://xlink.rsc.org/DOI=C6LC00367B.

[18] A.G. Niculescu, C. Chircov, A.C. Bîrcă, A.M. Grumezescu, Fabrication and applications of microfluidic devices: A review, 22, (ISSN: 14220067) 2021, pp. 1–26, http://dx.doi.org/10.3390/ijms22042011,

[19] X. Zhang, A. Liu, Y. Wang, C. Niu, X. Rong, C. Jia, J. Sun, S. Song, L. Zhang, F. Ye, C. Shao, M. Chu, Advancements and future perspectives of microfluidic technology in pediatric healthcare, Smart Med. 4 (3) (2025) http://dx.doi.org/10.1002/smmd.70018.

[20] Z. Chen, S. Kheiri, E.W.K. Young, E. Kumacheva, Trends in droplet microfluidics: From droplet generation to biomedical applications, Langmuir 38 (2022) 6233–6248, http://dx.doi.org/10.1021/acs.langmuir.2c00491, URL https://pubs.acs.org/doi/10.1021/acs.langmuir.2c00491.

[21] M.-Z. Jiang, H.-Z. Zhu, N. Zhou, C. Liu, C.-Y. Jiang, Y. Wang, S.-J. Liu, Droplet microfluidics-based high-throughput bacterial cultivation for validation of taxon pairs in microbial co-occurrence networks, Sci. Rep. 12 (1) (2022) 18145, http://dx.doi.org/10.1038/s41598-022-23000-7.

[22] C. Liu, X. Xu, Droplet microfluidics for advanced single-cell analysis, Smart Med. 4 (2) (2025) http://dx.doi.org/10.1002/smmd.70002.

[23] C.B. Chang, J.N. Wilking, S.-H. Kim, H.C. Shum, D.A. Weitz, Monodisperse emulsion drop microenvironments for bacterial biofilm growth, Small 11 (2015) 3954–3961, http://dx.doi.org/10.1002/smll.201403125, URL https://onlinelibrary.wiley.com/doi/10.1002/smll.201403125.

[24] Y. Tang, X. Cao, R. Kong, X. Li, J. Wang, J. Wu, X. Wang, Trajectory analysis of Bacillus subtilis in micro-droplets, Biomicrofluidics 18 (5) (2024) 054111, http://dx.doi.org/10.1063/5.0211134.

[25] H. Liu, L. Nan, F. Chen, Y. Zhao, Y. Zhao, Functions and applications of artificial intelligence in droplet microfluidics, Lab A Chip 23 (2023) 2497–2513, http://dx.doi.org/10.1039/D3LC00224A, URL http://xlink.rsc.org/?DOI=D3LC00224A.

[26] Z. Gao, Y. Li, Enhancing single-cell biology through advanced AI-powered microfluidics, Biomicrofluidics 17 (5) (2023) http://dx.doi.org/10.1063/5.0170050.

[27] J. Zhou, J. Dong, H. Hou, L. Huang, J. Li, High-throughput microfluidic systems accelerated by artificial intelligence for biomedical applications, Lab A Chip 24 (5) (2024) 1307–1326, http://dx.doi.org/10.1039/d3lc01012k.

[28] S. Panigrahi, D. Murat, A. Le Gall, E. Martineau, K. Goldlust, J.B. Fiche, S. Rombouts, M. Nöllmann, L. Espinosa, T. Mignot, MiSiC: a general deep learning-based method for the high-throughput cell segmentation of complex bacterial communities, ELife 10 (2021) e65151, http://dx.doi.org/10.7554/eLife.65151.

[29] M. Cicatka, R. Burget, J. Karasek, J. Lancos, Increasing segmentation performance with synthetic agar plate images, Heliyon 10 (3) (2024) e25714, http://dx.doi.org/10.1016/j.heliyon.2024.e25714.

[30] D. Abeyrathna, S. Rauniyar, R.K. Sani, P.-C. Huang, A morphological post-processing approach for overlapped segmentation of bacterial cell images, Mach. Learn. Knowl. Extr. 4 (4) (2022) 1024–1041, http://dx.doi.org/10.3390/make4040052, URL https://www.mdpi.com/2504-4990/4/4/52.

[31] M. Zhang, Z. Yang, Y. Wang, X. Ruan, Y. Zou, Y. Gao, H. Wang, N. Fang, Non-invasive single-cell morphometry in living bacterial biofilms, Nat. Commun. 11 (1) (2020) 6158, http://dx.doi.org/10.1038/s41467-020-19866-8.

[32] A. Kozlov, A. Yakimovich, E. Dultz, M. Wang, K.N. Kragh, T. Tolker-Nielsen, S.G. Stahlhut, H. Jespersen, A. Gill, J. Schindelin, M. Levin, U.J. Birk, Digital biology approach for macroscale studies of biofilm growth and biocide effects with electron microscopy, Digit. Discov. 2 (2) (2023) 420–432, http://dx.doi.org/10.1039/D3DD00048F.

[33] J. Zhang, Y. Wang, E.D. Donarski, T.T. Toma, M.T. Miles, S.T. Acton, A. Gahlmann, BCM3D 2.0: accurate segmentation of single bacterial cells in dense biofilms using computationally generated intermediate image representations, NPJ Biofilms Microbiomes 8 (1) (2022) 99, http://dx.doi.org/10.1038/s41522-022-00362-4.

[34] L. Liang, M. Liang, Z. Zuo, Y. Ai, Label-free single-cell analysis in microdroplets using a light-scattering-based optofluidic chip, Biosens. Bioelectron. 253 (2024) 116148, http://dx.doi.org/10.1016/j.bios.2024.116148.

[35] T. Vanhoucke, A. Perima, L. Zolfanelli, P. Bruhns, M. Broketa, Deep learning enabled label-free microfluidic droplet classification for single cell functional assays, Front. Bioeng. Biotechnol. 12 (2024) http://dx.doi.org/10.3389/fbioe.2024.1468738.
[36] J. Chen, L. Fu, R. Xiang, S. Luo, X. Huang, H. Yu, L. Sun, Artificial intelligence-assisted microfluidic bio-imaging—From sensors to applications: A review, IEEE Sensors J. 25 (2) (2025) 2056–2072, http://dx.doi.org/10.1109/jsen.2024.3507081.
[37] J. Cheng, R. Anne, Y.-C. Chen, Transforming microfluidics for single-cell analysis with robotics and artificial intelligence, Lab A Chip 25 (23) (2025) 6100–6125, http://dx.doi.org/10.1039/d5lc00216h.
[38] D.P. Kingma, M. Welling, Auto-encoding variational Bayes, in: Proceedings of the 2nd International Conference on Learning Representations, ICLR, 2014, arXiv:1312.6114.
[39] G. Volpe, B. Midtvedt, J. Pineda, H.K. Moberg, H. Bachimanchi, J.B. Pereira, C. Manzo, Deep Learning Crash Course, No Starch Press, San Francisco, CA, 2025.
[40] H.-J. Gu, Q.-L. Sun, J.-C. Luo, J. Zhang, L. Sun, A first study of the virulence potential of a Bacillus subtilis isolate from deep-sea hydrothermal vent, Front. Cell. Infect. Microbiol. 9 (2019) http://dx.doi.org/10.3389/fcimb.2019.00183, URL https://www.frontiersin.org/article/10.3389/fcimb.2019.00183/full.
[41] C. Feng, K. Takahashi, J. Zhu, Simple one-step and rapid patterning of PDMS microfluidic device wettability for PDMS shell production, Front. Bioeng. Biotechnol. 10 (2022) http://dx.doi.org/10.3389/fbioe.2022.891213, URL https://www.frontiersin.org/articles/10.3389/fbioe.2022.891213/full.
[42] N.E. Najjar, M.C.V. Teeseling, B. Mayer, S. Hermann, M. Thanbichler, P.L. Graumann, Bacterial cell growth is arrested by violet and blue, but not yellow light excitation during fluorescence microscopy, BMC Mol. Cell Biology 21 (2020) http://dx.doi.org/10.1186/s12860-020-00277-y.
[43] D.M. Harris, Spectra of pathogens predict lethality of blue light photoinactivation, Laser Ther. 30 (2023) 9–19, http://dx.doi.org/10.4081/ltj.2023.314.
[44] O. Kim, S.W. Kim, J.S. Kim, W.B. Lim, S.M. Jeon, O.S. Kim, J.T. Koh, C.S. Kim, H.R. Choi, In vitro bactericidal effects of 625, 525, and 425 nm wavelength (red, green, and blue) light-emitting diode irradiation, Photomed. Laser Surg. 31 (2013) 554–562, http://dx.doi.org/10.1089/pho.2012.3343.
[45] B. Midtvedt, J. Pineda, H. Klein Morberg, H. Bachimanchi, M. Granfors, A. Lech, C. Manzo, G. Volpe, Deeplay, URL https://github.com/DeepTrackAI/deeplay.
[46] N.C. Shaner, G.H. Patterson, M.W. Davidson, Advances in fluorescent protein technology, J. Cell Sci. 120 (24) (2007) 4247–4260, http://dx.doi.org/10.1242/jcs.005801.
[47] R.Y. Tsien, THE GREEN fluorescent PROTEIN, Annu. Rev. Biochem. 67 (1) (1998) 509–544, http://dx.doi.org/10.1146/annurev.biochem.67.1.509.
[48] The jamovi project, Jamovi (version 2.6) [computer software], 2024, URL https://www.jamovi.org.
[49] R.C. Team, R: A language and environment for statistical computing (version 4.4) [computer software], 2024, URL https://cran.r-project.org R packages retrieved from CRAN snapshot 2024-08-07.
[50] J. Fox, S. Weisberg, Car: Companion to applied regression [r package], 2023, URL https://cran.r-project.org/package=car.
[51] D.J. Collins, A. Neild, A. deMello, A.-Q. Liu, Y. Ai, The Poisson distribution and beyond: methods for microfluidic droplet production and single cell encapsulation, Lab A Chip 15 (17) (2015) 3439–3459, http://dx.doi.org/10.1039/c5lc00614g.
[52] D. Higgins, J. Dworkin, Recent progress inBacillus subtilissporulation, FEMS Microbiol. Rev. 36 (1) (2012) 131–148, http://dx.doi.org/10.1111/j.1574-6976.2011.00310.x.
[53] W.F. Burkholder, A.D. Grossman, Regulation of the initiation of endospore formation inBacillus subtilis, in: Prokaryotic Development, ASM Press, 2014, pp. 151–166, http://dx.doi.org/10.1128/9781555818166.ch7.
[54] S. Müller, S.N. Strack, S.E. Ryan, D.B. Kearns, J.R. Kirby, Predation by myxococcus xanthus induces Bacillus subtilis to form spore-filled megastructures, Appl. Environ. Microbiol. 81 (1) (2015) 203–210, http://dx.doi.org/10.1128/aem.02448-14.
[55] A.D. Grossman, R. Losick, Extracellular control of spore formation in Bacillus subtilis., Proc. Natl. Acad. Sci. 85 (12) (1988) 4369–4373, http://dx.doi.org/10.1073/pnas.85.12.4369.
[56] C.P. Aires, A.C. Polizello, A. Caliri, S. Mascarenhas, Bacillus subtilis engagement induced via sporulation: a case of bacterial communication, Braz. J. Phys. 52 (3) (2022) http://dx.doi.org/10.1007/s13538-022-01079-7.
[57] M.A. Hamon, B.A. Lazazzera, The sporulation transcription factor Spo0A is required for biofilm development in Bacillus subtilis, Mol. Microbiol. 42 (2001) 1199–1209, http://dx.doi.org/10.1046/j.1365-2958.2001.02709.x, URL https://onlinelibrary.wiley.com/doi/10.1046/j.1365-2958.2001.02709.x.
[58] P.J. Piggot, D.W. Hilbert, Sporulation of Bacillus subtilis, Curr. Opin. Microbiol. 7 (2004) 579–586, http://dx.doi.org/10.1016/j.mib.2004.10.001.
[59] D. Lindsay, V. Brözel, A.V. Holy, Spore formation in Bacillus subtilis biofilms, J. Food Prot. 68 (2005) 860–865, http://dx.doi.org/10.4315/0362-028X-68.4.860.
[60] I. Liaqat, S.I. Ahmed, N. Jahan, Biofilm formation and sporulation in Bacillus subtilis, Int. J. Microbiol. Res. Rev. 1 (2013) 61–67, No DOI available.
[61] B. Lories, S. Roberfroid, L. Dieltjens, D.D. Coster, K.R. Foster, H.P. Steenackers, Biofilm bacteria use stress responses to detect and respond to competitors, Curr. Biology 30 (2020) 1231–1244.e4, http://dx.doi.org/10.1016/j.cub.2020.01.065, URL https://linkinghub.elsevier.com/retrieve/pii/S0960982220301093.
[62] M. Seeger, R.J. Turner, M. González, An exploration of microbial response to stressors with prof. Claudio C. Vásquez Guzmán, Biol. Res. 55 (2022) 25, http://dx.doi.org/10.1186/s40659-022-00393-3.
[63] J. Majtan, L. Majtánová, M. Xu, V. Majtán, In vitro effect of subinhibitory concentrations of antibiotics on biofilm formation by clinical strains of Salmonella enterica serovar Typhimurium isolated in Slovakia, J. Appl. Microbiol. 104 (2008) 1294–1301, http://dx.doi.org/10.1111/j.1365-2672.2007.03653.x.
[64] D.L.R. Gomes, R.S. Peixoto, E.A.B. Barbosa, F. Napoleão, P.S. Sabbadini, K.R.N. dos Santos, A.L. Mattos-Guaraldi, R. Hirata, SubMICs of penicillin and erythromycin enhance biofilm formation and hydrophobicity of Corynebacterium diphtheriae strains, J. Med. Microbiol. 62 (2013) 754–760, http://dx.doi.org/10.1099/jmm.0.052373-0.
[65] J. Liang, T.Y. Huang, Y. Mao, X. Li, Biofilm formation of two genetically diverse Staphylococcus aureus isolates under beta-lactam antibiotics, Front. Microbiol. 14 (2023) http://dx.doi.org/10.3389/fmicb.2023.1139753.
[66] R. Bleich, J.D. Watrous, P.C. Dorrestein, A.A. Bowers, E.A. Shank, Thiopeptide antibiotics stimulate biofilm formation in Bacillus subtilis, Proc. Natl. Acad. Sci. 112 (2015) 3086–3091, http://dx.doi.org/10.1073/pnas.1414272112.
[67] Y. Liu, S. Kyle, P.D. Straight, Antibiotic stimulation of a Bacillus subtilis migratory response, MSphere 3 (2018) http://dx.doi.org/10.1128/mSphere.00586-17.
[68] K. Ochi, E. Freese, Effect of antibiotics on sporulation caused by the stringent response in Bacillus subtilis, Microbiol. 129 (1983) 3709–3720, http://dx.doi.org/10.1099/00221287-129-12-3709, URL https://www.microbiologyresearch.org/content/journal/micro/10.1099/00221287-129-12-3709.
[69] M. Macia, E. Rojo-Molinero, A. Oliver, Antimicrobial susceptibility testing in biofilm-growing bacteria, Clin. Microbiol. Infect. 20 (2014) 981–990, http://dx.doi.org/10.1111/1469-0691.12651, URL https://linkinghub.elsevier.com/retrieve/pii/S1198743X14653647.
[70] L. Thieme, A. Hartung, K. Tramm, M. Klinger-Strobel, K.D. Jandt, O. Makarewicz, M.W. Pletz, MBEC versus MBIC: The lack of differentiation between biofilm reducing and inhibitory effects as a current problem in biofilm methodology, 21, (ISSN: 14809222) 2019, http://dx.doi.org/10.1186/s12575-019-0106-0,
[71] K. Kobayashi, Bacillus subtilis pellicle formation proceeds through genetically defined morphological changes, J. Bacteriol. 189 (2007) 4920–4931, http://dx.doi.org/10.1128/JB.00157-07, URL https://journals.asm.org/doi/10.1128/JB.00157-07.
[72] S.B. Guttenplan, D.B. Kearns, Regulation of flagellar motility during biofilm formation, FEMS Microbiol. Rev. 37 (2013) 849–871, http://dx.doi.org/10.1111/1574-6976.12018, URL https://academic.oup.com/femsre/article-lookup/doi/10.1111/1574-6976.12018.
[73] V.M. Worlitzer, A. Jose, I. Grinberg, M. Bär, S. Heidenreich, A. Eldar, G. Ariel, A. Be'er, Biophysical aspects underlying the swarm to biofilm transition, Sci. Adv. 8 (2022) 8152, http://dx.doi.org/10.1126/sciadv.abn8152, URL https://www.science.org/doi/10.1126/sciadv.abn8152.
[74] H. Boudarel, J.-D. Mathias, B. Blaysat, M. Grédiac, Towards standardized mechanical characterization of microbial biofilms: analysis and critical review, Npj Biofilms Microbiomes 4 (1) (2018) 17.
[75] K. Sauer, P. Stoodley, D.M. Goeres, L. Hall-Stoodley, M. Burmølle, P.S. Stewart, T. Bjarnsholt, The biofilm life cycle: expanding the conceptual model of biofilm formation, Nat. Rev. Microbiol. 20 (10) (2022) 608–620.
[76] K.N. Kragh, T. Tolker-Nielsen, M. Lichtenberg, The non-attached biofilm aggregate, Commun. Biol. 6 (1) (2023) 898.
[77] G. Melaugh, J. Hutchison, K.N. Kragh, Y. Irie, A. Roberts, T. Bjarnsholt, S.P. Diggle, V.D. Gordon, R.J. Allen, Shaping the growth behaviour of biofilms initiated from bacterial aggregates, PloS One 11 (3) (2016) e0149683.
[78] J. Kim, H.-D. Park, S. Chung, Microfluidic approaches to bacterial biofilm formation, Molecules 17 (8) (2012) 9818–9834.
[79] H. Jang, R. Rusconi, R. Stocker, Biofilm disruption by an air bubble reveals heterogeneous age-dependent detachment patterns dictated by initial extracellular matrix distribution, Npj Biofilms Microbiomes 3 (1) (2017) 6.
[80] R. Nijland, M.J. Hall, J.G. Burgess, Dispersal of biofilms by secreted, matrix degrading, bacterial dnase, PloS One 5 (12) (2010) e15668.
[81] A.L. Ibáñez de Aldecoa, O. Zafra, J.E. González-Pastor, Mechanisms and regulation of extracellular DNA release and its biological roles in microbial communities, Front. Microbiol. 8 (2017) 1390.
[82] Á.T. Kovács, N.R. Stanley-Wall, Biofilm dispersal for spore release in Bacillus subtilis., J. Bacteriol. 203 (2021) e0019221, http://dx.doi.org/10.1128/JB.00192-21, http://www.ncbi.nlm.nih.gov/pubmed/33927051 http://www.pubmedcentral.nih.gov/articlerender.fcgi?artid=PMC8223919.
[83] V.L. Marlow, F.R. Cianfanelli, M. Porter, L.S. Cairns, J.K. Dale, N.R. Stanley-Wall, The prevalence and origin of exoprotease-producing cells in the Bacillus subtilis biofilm, Microbiology 160 (1) (2014) 56–66.
[84] Á.T. Kovács, A. Dragoš, Evolved biofilm: review on the experimental evolution studies of Bacillus subtilis pellicles, J. Mol. Biol. 431 (23) (2019) 4749–4759.

[85] J. van Gestel, H. Vlamakis, R. Kolter, New tools for comparing microscopy images: Quantitative analysis of cell types in Bacillus subtilis, J. Bacteriol. 197 (4) (2015) 699–709, http://dx.doi.org/10.1128/JB.02501-14.

[86] S. Gingichashvili, D. Duanis-Assaf, M. Shemesh, J.D.B. Featherstone, O. Feuerstein, D. Steinberg, Bacillus subtilis biofilm development – a computerized study of morphology and kinetics, Front. Microbiol. 8 (2017) 2072, http://dx.doi.org/10.3389/fmicb.2017.02072.

[87] R. Hartmann, H. Jeckel, C. Jelli, S. Singh, P.K. Vaidya, A. Hölscher, D.K. Nedelcu, K. Paarmann, N. Vidakovic, C.J. Nadell, J. Drescher, Quantitative image analysis of microbial communities with BiofilmQ, Nat. Microbiol. 6 (2021) 151–156, http://dx.doi.org/10.1038/s41564-020-00817-4.

[88] C. Guilhen, C. Forestier, D. Balestrino, Biofilm dispersal: multiple elaborate strategies for dissemination of bacteria with unique properties, Mol. Microbiol. 105 (2017) 188–210, http://dx.doi.org/10.1111/mmi.13698, URL https://onlinelibrary.wiley.com/doi/10.1111/mmi.13698.

[89] M. Bartolini, S. Cogliati, D. Vileta, C. Bauman, L. Rateni, C. Leñini, F. Argañaraz, M. Francisco, J.M. Villalba, L. Steil, U. Völker, R. Grau, Regulation of biofilm aging and dispersal in Bacillus subtilis by the alternative sigma factor sigb, J. Bacteriol. 201 (2019) http://dx.doi.org/10.1128/JB.00473-18, URL https://journals.asm.org/doi/10.1128/JB.00473-18.

[90] M. Nishikawa, K. Kobayashi, Calcium prevents biofilm dispersion in Bacillus subtilis, J. Bacteriol. 203 (2021) http://dx.doi.org/10.1128/JB.00114-21, URL https://journals.asm.org/doi/10.1128/JB.00114-21.

[91] R. Zhao, Y. Song, Q. Dai, Y. Kang, J. Pan, L. Zhu, L. Zhang, Y. Wang, X. Shen, A starvation-induced regulator, RovM, acts as a switch for planktonic/biofilm state transition in Yersinia pseudotuberculosis, Sci. Rep. 7 (2017) 639, http://dx.doi.org/10.1038/s41598-017-00534-9, http://www.nature.com/articles/s41598-017-00534-9.

[92] Y. Ma, Y. Deng, H. Hua, B.L. Khoo, S.L. Chua, Distinct bacterial population dynamics and disease dissemination after biofilm dispersal and disassembly, ISME J. 17 (2023) 1290–1302, http://dx.doi.org/10.1038/s41396-023-01446-5, URL https://academic.oup.com/ismej/article/17/8/1290-1302/7505834.

[93] J.E. González-Pastor, Cannibalism: a social behavior in sporulating Bacillus subtilis, FEMS Microbiol. Rev. 35 (3) (2011) 415–424.

[94] A. Lamsa, W.-T. Liu, P.C. Dorrestein, K. Pogliano, The Bacillus subtilis cannibalism toxin SDP collapses the proton motive force and induces autolysis, Mol. Microbiol. 84 (3) (2012) 486–500.

[95] D. López, H. Vlamakis, R. Losick, R. Kolter, Cannibalism enhances biofilm development in Bacillus subtilis, Mol. Microbiol. 74 (3) (2009) 609–618.

[96] M. Gjermansen, P. Ragas, C. Sternberg, S. Molin, T. Tolker-Nielsen, Characterization of starvation-induced dispersion in pseudomonas putida biofilms, Environ. Microbiol. 7 (2005) 894–904, http://dx.doi.org/10.1111/j.1462-2920.2005.00775.x, URL https://onlinelibrary.wiley.com/doi/10.1111/j.1462-2920.2005.00775.x.

[97] M. Harmsen, L. Yang, S.J. Pamp, T. Tolker-Nielsen, An update on pseudomonas aeruginosa biofilm formation, tolerance, and dispersal, FEMS Immunol. Med. Microbiol. 59 (2010) 253–268, http://dx.doi.org/10.1111/j.1574-695X.2010.00690.x, URL https://academic.oup.com/femspd/article-lookup/doi/10.1111/j.1574-695X.2010.00690.x.

[98] W. Zhang, A. Seminara, M. Suaris, M.P. Brenner, D.A. Weitz, T.E. Angelini, Nutrient depletion in Bacillus subtilis biofilms triggers matrix production, New J. Phys. 16 (2014) 015028, http://dx.doi.org/10.1088/1367-2630/16/1/015028, URL https://iopscience.iop.org/article/10.1088/1367-2630/16/1/015028.

[99] L. Hobley, S.H. Kim, Y. Maezato, S. Wyllie, A.H. Fairlamb, N.R. Stanley-Wall, A.J. Michael, Norspermidine is not a self-produced trigger for biofilm disassembly, Cell 156 (2014) 844–854, http://dx.doi.org/10.1016/j.cell.2014.01.012, URL https://linkinghub.elsevier.com/retrieve/pii/S0092867414000233.

[100] S.-K. Kim, J.-H. Lee, Biofilm dispersion in pseudomonas aeruginosa, J. Microbiol. 54 (2016) 71–85, http://dx.doi.org/10.1007/s12275-016-5528-7, URL http://link.springer.com/10.1007/s12275-016-5528-7.

[101] S.S. Branda, J.E. González-Pastor, S. Ben-Yehuda, R. Losick, R. Kolter, Fruiting body formation by Bacillus subtilis, Proc. Natl. Acad. Sci. USA 98 (20) (2001) 11621–11626, http://dx.doi.org/10.1073/pnas.191384198.

[102] R.M. Losick, Bacillus subtilis: a bacterium for all seasons, Curr. Biol. 30 (2020) R1146–R1150, http://dx.doi.org/10.1016/j.cub.2020.06.083, URL https://linkinghub.elsevier.com/retrieve/pii/S0960982220309350.

[103] Q.O. Ababneh, J.K. Herman, Rela inhibits Bacillus subtilis motility and chaining, J. Bacteriol. 197 (1) (2015) 128–137, http://dx.doi.org/10.1128/jb.02063-14, arXiv:https://journals.asm.org/doi/pdf/10.1128/jb.02063-14 URL https://journals.asm.org/doi/abs/10.1128/jb.02063-14.

[104] Y. Chai, F. Chu, R. Kolter, R. Losick, Bistability and biofilm formation in Bacillus subtilis, Mol. Microbiol. 67 (2) (2008) 254–263, http://dx.doi.org/10.1111/j.1365-2958.2007.06040.x, arXiv:https://onlinelibrary.wiley.com/doi/pdf/10.1111/j.1365-2958.2007.06040.x URL https://onlinelibrary.wiley.com/doi/abs/10.1111/j.1365-2958.2007.06040.x.

[105] M. Shemesh, Y. Chai, A combination of glycerol and manganese promotes biofilm formation in Bacillus subtilis via histidine kinase kind signaling, J. Bacteriol. 195 (12) (2013) 2747–2754, http://dx.doi.org/10.1128/JB.00028-13.